

## Asymmetric wake of a horizontal cylinder in close proximity to a solid boundary for Reynolds numbers in the subcritical turbulence regime

Pablo Ouro <sup>\*</sup>, Valentine Muhawenimana,<sup>†</sup> and Catherine A. M. E. Wilson<sup>‡</sup>  
*Hydro-environmental Research Centre, School of Engineering, Cardiff University,  
Cardiff CF24 3AA, United Kingdom*



(Received 20 December 2018; published 15 October 2019)

The near-wake dynamics developed behind a horizontal cylinder with wall proximity effects are elucidated from laboratory experiments and large-eddy simulations (LES). Fixed vertical gap to diameter ( $G/D$ ) ratios of 0.5 and 1.0 were investigated for Reynolds numbers equal to 6666, 10000, and 13333. The LES results agreed well with the experimental measurements for the time-averaged flow quantities and captured the upward flow motion developed over the lower half of the flow depth as a consequence of the near-wall effect. The presence of a narrow gap between the cylinder and the bed, i.e.,  $G/D = 0.5$ , significantly influenced the dynamics of the vortex generation and shedding which, in consequence, led to an increasingly pronounced asymmetric wake distribution with increasing Reynolds number. In the wider gap case of  $G/D = 1.0$ , the wake remained relatively symmetrical, with reduced impact of ground proximity. Kelvin-Helmholtz instabilities developed in the upper and lower shear layers were shown to be decoupled as their instantaneous laminar-to-turbulent transition occurred at different downstream distances at any given time. Spanwise rollers were shown to form with an undulating pattern and presented irregularly located vortex dislocations. Furthermore, a ground vortex induced during the early stages of the lower roller's generation in the wake lifted off the ground and merged with the von Kármán vortices to form a single vortical structure. For  $G/D = 0.5$ , a positive upwards force was present, and experimental and LES Strouhal number values ranged between 0.28–0.32, while computed drag coefficient values were lower than those typical for unbounded cylinder flows. As for  $G/D = 1.0$ , Strouhal numbers decrease to a 0.26–0.30 range while drag coefficient increases, further demonstrating the effects on the cylinder wake structure dynamics due to the proximity to a solid boundary.

DOI: [10.1103/PhysRevFluids.4.104604](https://doi.org/10.1103/PhysRevFluids.4.104604)

### I. INTRODUCTION

The wake structure around a vertically orientated cylinder has been the subject of research for more than a century due to the abundance of curved bodies in nature as well as in civil, mechanical, and aeronautical engineering. Recent research efforts have also focused on the flow structure in the wake of a horizontal-orientated cylinder [1,2], i.e., its main axis is parallel to a close wall and perpendicular to the flow direction as depicted in Fig. 1. The dependency of the wake dynamics on the Reynolds number ( $Re = UD/\nu$ ) has been studied extensively for vertical cylinders and to a lesser extent for horizontal cylinders. This knowledge is critical to our understanding of how the dynamic forces imposed by the fluid on the body change as a function of flow regime and fluid viscosity, as pertaining to fluid-body interactions.

---

<sup>\*</sup>ourop@cardiff.ac.uk

<sup>†</sup>muhawenimanav@cardiff.ac.uk

<sup>‡</sup>wilsonca@cardiff.ac.uk

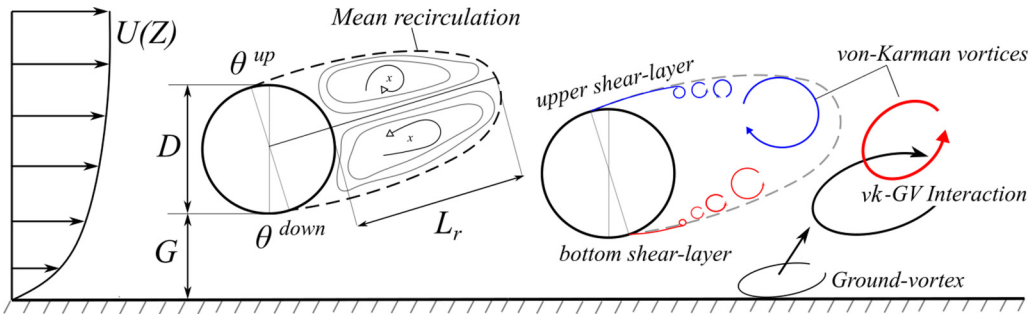


FIG. 1. Schematic of the wake dynamics in horizontal cylinder flows in proximity to a wall and with logarithmic approaching velocity profile. The main instantaneous wake dynamics phenomena, such as the ground-vortex (GV) or von Kármán vortices (VK), are depicted together with the time-averaged wake characteristics, such as recirculation length  $L_r$ , separation angles  $\theta$ .

Flow around a horizontal cylinder can exhibit different behavior compared to a vertical cylinder, depending on the flow conditions in which is embedded, such as in a boundary layer flows [1], or be influenced by its proximity to the ground [2]; resulting in altered wake dynamics as shown in Fig. 1. Some of these changes are related to asymmetric vortex shedding, modification of the separation angles or the appearance of a ground vortex. This ground vortex notably interacts with the von Kármán vortices shed from the bottom shear layer as these turbulent structures feature an opposite vorticity sign [3].

Nonetheless, the Reynolds number governs the flow features developed around both vertically and horizontally oriented cylinders. Several laboratory experiments and numerical simulations focusing on the subcritical flow regime ( $3 \times 10^2 < Re < 1 \times 10^5$ ) have highlighted the higher shedding frequency of the shear layer generated vortices ( $f_{SL}$ ) compared to that of the large-scale von Kármán-type (VK) vortices ( $f_K$ ), where the frequency of the former vortices can occur at a factor of 6.7 to 8.0 times greater than the wake ones [4–7], and Prasad and Williamson [8] demonstrated the correlation between the ratio  $f_{SL}/f_K$  and Reynolds number. Furthermore, at Reynolds number around 1 200 the shear layers separating from the cylinder’s sides become unstable undergoing laminar-to-turbulent transition due to Kelvin-Helmholtz instability [8]. A transition in the subcritical wake dynamics occurs at a Reynolds number around 5 000 to 5 500 where a distinct change in the shedding typology has been observed in both experimental and numerical studies [7–9]. This transition is distinguished by the presence of undulations in the vortex filaments shedding across the cylinder span and the occurrence of vortex dislocations [7,9] which also leads to a change from parallel to oblique vortex shedding [8]. With increasing Reynolds number greater than 5 000 the wake typology remains unchanged up to a Reynolds number of  $2 \times 10^5$ , which marks the beginning of the supercritical flow regime where a significant change in the flow separation reduces the drag coefficient from values ranging from 1.0–1.4 to 0.2–0.4 [10–12]. A detailed summary of the wake dynamics dependency on Reynolds number is given in Williamson [13] and Sumner [14].

A cylindrical body is often in close proximity of a solid boundary, for example, a pipeline across an erodible river or sea bed, a bridge pier close to an abutment or a mast located close to a building. Only a few studies have examined the close proximity of a solid boundary on a horizontal cylinder wake’s flow structure [1–3,15–19]. In this configuration, the ratio of the horizontal cylinder diameter ( $D$ ) and the vertical gap between the bottom wall and the cylinder ( $G$ ), referred to hereafter as the gap ratio ( $G/D$ ), is highly influential on the vortex dynamics developed downstream. For small gap ratios, e.g.,  $G/D \leq 0.5$ , the wake is asymmetric as a result of the difference in acceleration of the flow over and under the cylinder, and the interaction of the under flow with the wall boundary layer. As the gap ratio decreases, the ground effect increases, which causes the separation point on the upper cylinder wall to move upstream while the separation point on the lower cylinder wall

moves downstream [3]. Furthermore, the frontal stagnation point moves toward the bottom wall and an upwards force which increases with decreasing gap ratio is generated on the cylinder [1,20,21] while the lower vortex is drawn upwards in the vertical direction immediately behind the cylinder [2,3]. This leads to a separation bubble forming close to the bottom bed immediately downstream of the wake bubble, which rapidly reduces in vertical and longitudinal extent with increasing gap ratio [3]. At smaller gap ratios ( $G/D = 0.25$ ) and relatively low Reynolds numbers, a bubble can also be formed at the wall immediately upstream of the cylinder which rapidly reduces in extent with increasing  $G/D$  ratio [3]. As the gap ratio approaches unity, the ground effect vanishes causing the flow separation sequence and the recirculation bubble to become more symmetric, i.e., the upper and lower laminar shear layers becoming unstable at a similar distances downstream [2,3].

The proximity of the wall alters the hydrodynamic forces on the horizontal cylinder and the von Kármán-type vortex shedding frequency depends on both the thickness of the boundary layer and the gap ratio [22,23]. The upwards force on the cylinder is accompanied by a reduction in the drag coefficient which decreases with decreasing gap ratio [21]. The proximity of the wall also alters the dominant vortex shedding frequency, resulting in complex vortex-boundary interactions. At lower Reynolds numbers ( $1.2 \times 10^3 < Re < 1.44 \times 10^3$ ) and gap ratios ( $G/D < 0.5$ ), two distinct peaks observed in the power spectra of the root-mean-square streamwise velocity have been attributed to the difference in motion between the upper and lower vortices shed from the upper and lower cylinder sides respectively, resulting in vortex-boundary interactions different from the unbounded cylinder condition [3,16]. Indeed, for smaller gap ratios, the rms of the fluctuating lift coefficient is significantly lower for higher  $G/D$  ratios as a consequence of the suppression of the VK vortex shedding at the smaller  $G/D$  ratios [3]. The higher values of Strouhal number reported in these studies than those from unbounded cylinder flow are therefore a result of the different development of the vortex shedding and shear layers instability. With increasing gap ratio, the two peaks in the shedding frequency merge into one single dominant peak [3] and periodic symmetric vortex shedding occurs. Hence, at a critical gap ratio in the range of  $0.5 \leq G/D \leq 1.0$ , the Strouhal number becomes independent of the gap ratio, approaching a value of around 0.2 commonly found in cylinder flows unaffected by boundary effects [3,16,21,24,25].

Additionally, at higher Reynolds numbers ( $4 \times 10^4 < Re < 1 \times 10^5$ ) a small gap ratio can not only suppress VK vortex shedding but completely stop it [1]. For a cylinder with aspect ratio ( $L/D$ ) of 8.33, the VK vortex shedding becomes intermittent at a gap ratio of 0.4 before completely ceasing at a gap ratio of 0.3. At this lower gap ratio, a larger recirculation zone is bounded by two nearly parallel shear layers from the cylinder sides, with no VK vortices observed and only small-scale vortices generated from shear layers. The change in wake dynamics at a gap ratio of 0.3 is reflected in the drag coefficient reduction, which reaches a minimum at this gap ratio, and remains constant with decreasing  $G/D$  ratio [1].

Irrespective of the experimental measurement technique and numerical model, it is commonly agreed that the accurate measurement and prediction of the time-averaged high-order flow statistics in the near wake is highly challenging [6,14,26]. It has been postulated that there are different modes of low-frequency meandering of the near wake that may be responsible for the large scattering of flow statistics [6], which need to be resolved together with the high-frequency turbulence in the flow. Therefore, emphasis has been placed on the need to perform direct numerical simulations (DNS) or large-eddy simulations (LES) capable of resolving these flow characteristics conducted over a large number of shedding cycles in order to capture all the high- and low-frequency periodic motions. Numerical studies using LES and DNS have identified the wake's three-dimensionality by using different spanwise-length domains to capture the wavelength of the vortical structures across the cylinder span. For Reynolds numbers lower than 5 000, a minimum spanwise length of  $2\pi D$  is required to accurately capture even the longest wavelengths developed in the wake, which can influence the dynamic forces on the cylinder [7], whereas a spanwise length of  $\pi D$  would only capture the turbulence structures in the shear layer and near-wake regions [6,27,28].

There are few experimental and numerical test cases that have investigated a horizontal cylinder wake in the close proximity of a bottom wall boundary at moderate Reynolds numbers. The

TABLE I. Details of the flow conditions studied: flow discharge ( $Q$ ), Reynolds number based on cylinder diameter ( $Re$ ), bulk Reynolds number ( $Re_R$ ), bulk velocity ( $U_0$ ), Froude number ( $Fr$ ), and estimated friction velocity ( $u_*$ ).

$Q$ [ $ls^{-1}$ ]	$Re$	$Re_R$	$U_0$ [ $ms^{-1}$ ]	$Fr$	$u_*$ [ $ms^{-1}$ ]
6	6 666	10 000	0.1333	0.110	0.020
9	10 000	15 000	0.2000	0.165	0.027
12	13 333	20 000	0.2667	0.220	0.033

present study combines an experimental study with high-fidelity large-eddy simulations (LES) to further elucidate the three-dimensional near-wake flow structure of a horizontal cylinder with wall proximity effects. The LES were conducted for gap ratios ( $G/D$ ) of 0.5 and 1.0 and for Reynolds numbers ( $Re$ ) equal to 6 666, 10 000 and 13 333 while the experimental tests were conducted for the smaller gap ratio ( $G/D = 0.5$ ). To the best of our knowledge, these specific gap ratios have not been investigated for Reynolds numbers higher than the threshold  $Re = 5 000$  at which there is a distinct shift in the vortex shedding dynamics found in cylinder flows unaffected by boundary effects.

## II. EXPERIMENTAL SETUP AND DATA PROCESSING

The experiments were conducted in a recirculating flume with glass sidewalls in the hydraulics laboratory at Cardiff University, United Kingdom. The flume had a rectangular cross-section, and was 10 m long, 0.3 m wide and 0.3 m deep. A horizontal cylinder of diameter ( $D$ ) 0.05 m and length 0.3 m was fixed 3.85 m downstream from the upstream inlet. The vertical gap ( $G$ ) between the flume bottom wall and the cylinder wall was 0.025 m giving a  $G/D$  ratio of 0.5. The flow structure in the cylinder wake was examined for three different flow discharges ( $Q$ ) of 6, 9, and 12  $ls^{-1}$ , which equated to cross-sectional bulk velocities of  $U_0 = 0.1333$ , 0.20 and 0.2667  $ms^{-1}$ , respectively. The mean flow depth ( $H$ ) along the flume center line remained fixed at 0.15 m for each flow condition and this was achieved by adjusting the downstream tailgate weir. The bed slope of the flume remained fixed at 1:1000. Table I presents details of the Reynolds numbers based on the cylinder diameter ( $Re = U_0 D / \nu$ ), bulk Reynolds number ( $Re_R = U_0 R / \nu$ , where  $R = A/P$  is the hydraulic radius,  $A$  is the cross-section area and  $P$  is the wetted perimeter) and Froude number [ $Fr = U_0 (gH)^{-0.5}$ , where  $g$  is the gravity acceleration] for the different flow conditions studied.

Velocity measurements were collected using a Nortek 10 MHz Vectrino Plus acoustic Doppler velocimeter (ADV) at a sampling rate of 200 Hz and 300 s sampling time. This time period of ADV measurements are equivalent to approx. 255 shedding cycles for  $Q = 6 ls^{-1}$  and 483 events for  $Q = 12 ls^{-1}$ , based on the frequencies shown later in Sec. IV F. The cylindrical sampling volume (6-mm diameter and 7-mm height) was located at 50 mm from the probe transmitter. Thresholds of sound-to-noise ratio (SNR) and correlation (COR)  $>20$  dB and  $>70\%$ , respectively, were maintained by seeding the water with silicate powder (10  $\mu m$  average diameter and 1.1  $kg m^{-3}$  density) and used for filtering the velocity time series. Despiking of time series used the Phase-Space Thresholding (PST) method by Goring and Nikora [29] as well as a 12-Point polynomial (12PP) [30]. Furthermore, by examining the velocity variances, data points identified as weak spots, which are errors resulting from acoustic pulse-to-pulse interference [31] were removed from the dataset. A velocity measurement grid resolution of 0.005 and 0.02 m was used in the vertical ( $z$ ) and streamwise ( $x$ ) directions, respectively, in the cylinder wake. This spatial resolution of the experimental data allowed effective capture of the dynamics of the wake structure. The velocity structure in the wake was measured along the channel center line over a downstream distance of 0.3 m, i.e.,  $6D$ . In the following, the symbols  $\langle \cdot \rangle$  indicates time-averaging operation.

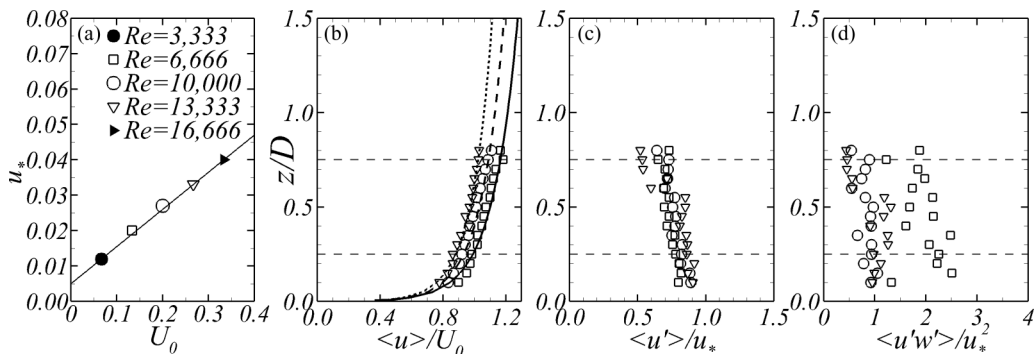


FIG. 2. Approaching inflow experimentally measured at a distance of  $3D$  upstream of the cylinder where (a) plots the bulk velocity ( $U_0$ ) against shear velocity ( $u_*$ ) derived from the velocity logarithmic profile fit [Eq. (1)] for five flow conditions ranging from  $3333 < Re < 16666$ ; and vertical profiles of: (b) time-averaged streamwise velocity normalized by the bulk velocity, (c) streamwise velocity fluctuation normalized by shear velocity, and (d) vertical Reynolds shear stress normalized by the shear velocity squared for the three Reynolds number modeled in this study.

### Approach flow conditions

At a longitudinal distance of three diameters ( $3D$ ) upstream of the cylinder, vertical velocity profiles ( $z$  direction) were measured as well as the lateral velocity distribution ( $y$  direction) at the midflow depth ( $0.5H$ ) to capture the upstream flow boundary conditions. Figure 2 presents a comparison of the measured approach flow profiles for the three discharges. The friction velocity ( $u_*$ ) was obtained from the best-fit of the velocity measurements to a log-law [Fig. 2(b)] that were measured for five flow conditions which included the three flow conditions modeled in this paper (i.e.,  $Re = 6666, 10000,$  and  $13333$ ). Figure 2(a) shows that the friction velocity increased linearly with the bulk velocity and thus the velocity profile approaching the cylinder can be defined according to a log-law distribution as

$$\frac{u(z)}{u_*} = \frac{1}{\kappa} \ln\left(\frac{zu_*}{\nu}\right), \quad \text{where } u_* = 0.1036U_0 + 0.00568 \quad (1)$$

Here  $\kappa$  is the von Kármán constant equal to 0.41,  $z$  is the vertical coordinate considered and  $\nu$  is the kinematic viscosity. Levels of streamwise velocity fluctuations were similar for all discharges, being largest close to the flume's bed and decreased with increasing elevation [Fig. 2(c)]. The depth-averaged turbulence intensity,  $\langle u' \rangle / U_0$ , was found to be around 10% for all cases. Figure 2(d) shows that values of the cross-correlation of streamwise and vertical velocity fluctuations were largest for the lowest Reynolds number ( $Re = 6666$ ) while similar magnitudes were found for the  $Re = 10000$  and  $13333$ . Velocities measurements in the transverse direction showed a negligible variation in streamwise velocities, therefore the flow was assumed uniform across the flume width.

## III. COMPUTATIONAL METHOD AND SETUP

### A. Numerical framework

Eddy-resolving simulations are accomplished using the in-house code Hydro3D which has been well-validated in hydraulic and environmental flows [32–37]. Hydro3D adopts the large-eddy simulation (LES) approach to explicitly resolve the energy-containing flow structures while modeling the scales smaller than the grid size using a subgrid scale model. The governing equations

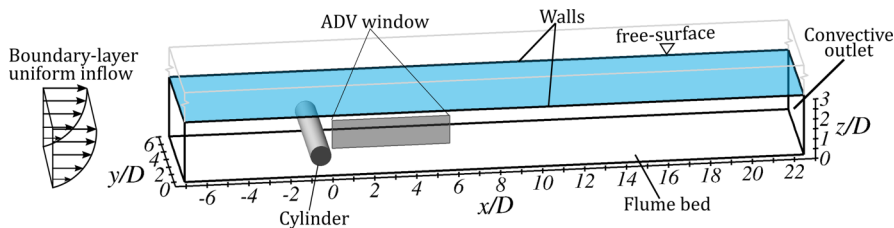


FIG. 3. Schematic of the computational domain with the imposed boundary conditions showing location of horizontal cylinder and laboratory ADV measurement control volume.

are the spatially filtered Navier-Stokes equations for incompressible, viscous flow that are solved in a Eulerian coordinate system, and are as follows:

$$\frac{\partial u_i}{\partial x_i} = 0, \quad (2)$$

$$\frac{\partial u_i}{\partial t} + \frac{\partial u_i u_j}{\partial x_j} = -\frac{\partial p}{\partial x_i} + \nu \frac{\partial^2 u_i}{\partial x_j \partial x_j} - \frac{\partial \tau_{ij}}{\partial x_j} + f_i. \quad (3)$$

Here,  $u_i = (u, v, w)$  and  $x_i = (x, y, z)$  are the filtered fluid velocity and position in the three coordinates of space respectively,  $p$  denotes filtered pressure,  $\nu$  is the fluid kinematic viscosity,  $\rho$  is the fluid density, and  $\tau_{ij}$  is the subgrid scale stresses. The subgrid scale stress tensor is approximated using the WALE subgrid scale model [38] considering a filter size equal to the grid size. The forcing term  $f_i$  represents external forces calculated using the direct forcing immersed boundary method [39], here used to represent the cylinder geometry [40].

In Hydro3D the fluxes are calculated using a pure second-order central differencing scheme with staggered storage of the velocity components on a rectangular Cartesian grid. The fractional-step method is used with a three-step Runge-Kutta predictor to approximate convective and diffusive terms, and an efficient multigrid technique is adopted to solve a Poisson pressure-correction equation as a corrector at the final step. Hydro3D uses the domain decomposition technique to divide the computational domain into rectangular subdomains and is parallelized with message passing interface (MPI) [41]. It also features a local mesh refinement method [42] that permits a higher spatial grid resolution near the cylinder and a coarser grid resolution with increasing distance away from the cylinder, thus reducing the computational expense.

## B. Computational setup

The schematic of the computational domain presented in Fig. 3 comprises  $30D$  in the streamwise direction,  $6D$  in the cross-streamwise direction, and  $3D$  in the vertical direction, therefore replicating the full flume width and the uniform flow depth used in the experiments. Note the spanwise domain length ( $6D$ ) is very close to the proposed length of  $2\pi D$  required to fully capture the spanwise wavelength of the vortical structures in the cylinder wake [7]. The downstream end of the cylinder is located  $7D$  from the upstream inlet and considered as the origin of the  $x$  coordinates. Two cylinder locations were studied with LES, one adopting the gap ratio as studied in the experimental study and another case with a gap ratio of 1.0, which is indicative of the case where the cylinder is unaffected by proximity to the bottom wall.

The same grid resolution is adopted for the two lower Reynolds numbers ( $Re = 6666$  and  $10000$ ), while the resolution is doubled for the highest Reynolds number case ( $Re = 13333$ ) due to an increase in the friction velocity and the requirement to keep the first grid cell off the wall within the viscous sublayer [43]. The grid resolution adopted is the same in  $x$  and  $z$  directions ( $\Delta x = \Delta z$ ), while it was doubled in the spanwise direction, i.e.,  $\Delta y = 2\Delta z$ . The resolution in the computational domain is non uniform in the streamwise direction, as local mesh refinement is adopted [42], but

TABLE II. Specification of the computational grid resolution used and total number of fluid cells for each of the cases analyzed.

Re	$U_0$ [ms <sup>-1</sup> ]	$\Delta z$ [m]	$\Delta z^+$	Grid cells
6666	0.1333	$6.250 \times 10^{-4}$	6.25	$14.32 \times 10^6$
10000	0.2000	$6.250 \times 10^{-4}$	8.44	$14.32 \times 10^6$
13333	0.2666	$3.125 \times 10^{-4}$	5.16	$82.94 \times 10^6$

uniform in the spanwise and vertical extensions. A fine grid size is adopted in the region embedding the cylinder and the near wake between  $x = -1D$  and  $5D$ , while the grid size is doubled in the remaining domain to reduce the computational burden of the simulations. Table II details the mesh resolution in the fine grid region ( $\Delta z$ ) for three flow conditions examined, grid resolution of the first cell off the wall in wall-units ( $\Delta z^+$ ), and millions of fluid cells comprising the entire computational domain. In the far wake after  $x/D > 20$ , the resolution in wall units of  $\Delta y^+$  and  $\Delta z^+$  reach values up to 2 and 18, respectively.

The log-law velocity profile [Eq. (1)] is prescribed at the inlet of the domain and adjusted for each of the examined flow discharges. A convective condition is used at the outlet and no-slip conditions were imposed at the bottom and lateral walls, which is justified from the values of  $\Delta z^+$ , indicating that the first point off the wall is within the viscous sublayer. A shear-free rigid-lid condition [44] is employed to represent the water surface as the influence of free-surface effects is considered small when the maximum Fr is relatively low (0.22), and this is defined as

$$\frac{\partial u}{\partial z} = 0, \quad \frac{\partial v}{\partial z} = 0, \quad w = 0, \quad \text{for } z = H \quad (4)$$

The simulations are initially run until flow transients have vanished. First order statistics are then collected for a total simulation time in terms of nondimensional time  $t^* = tD/U_0$  of 260 equating to 32 eddy turn-over time ( $t_e = H/u_*$ ). Second-order statistics are collected after  $t^* = 60$  for a total of  $200D/U_0$  representing approximately 170 shedding cycles. A Courant-Friedrichs-Lewy (CFL) condition of 0.7 is set to ensure numerical stability. The computations are performed on 170 Intel Skylake Gold 6148 @2.40 GHz cores using Supercomputing Wales facilities with a total computational load of 225 000 CPU hours for the highest Reynolds number case (Re = 13 333).

## IV. RESULTS AND DISCUSSION

### A. Time-averaged nature of the flow

Results of the time-averaged flow developed around the cylinder for the  $G/D$  and Re = 6666 case are shown in Fig. 4 along the channel center-line plane, i.e.,  $y/D = 3$ . The distribution of streamwise velocities evidences how the approaching flow impinges the cylinder and accelerates over and beneath it, as depicted from Fig. 4(a). Flow streamlines indicate that the recirculation area immediately behind the cylinder is mostly symmetric and extends until approximately  $1D$  downstream. After  $x/D = 1$ , the streamwise velocities significantly diminish outside of the wake bubble on the lower side of the wake, i.e.,  $z/D < 0.5$ , compared to the high-momentum region located above the wake ( $z/D = 1.5$ ). Figure 4(b) presents the contours of time-averaged vertical velocities showing the asymmetry in the flow influenced upstream by the logarithmic distribution of the approaching flow and downstream by the closer proximity of the cylinder to the channel bottom than free-surface layer. The area of high vertical velocities in the lower part of the near wake is a result of the bed effect as the fluid accelerates through the vertical gap between the cylinder and flume bed.

The lack of a more pronounced asymmetry in the recirculation bubble despite the small gap ratio  $G/D$  of 0.5 is somewhat expected as this  $G/D$  ratio corresponds to the intermediate range in which

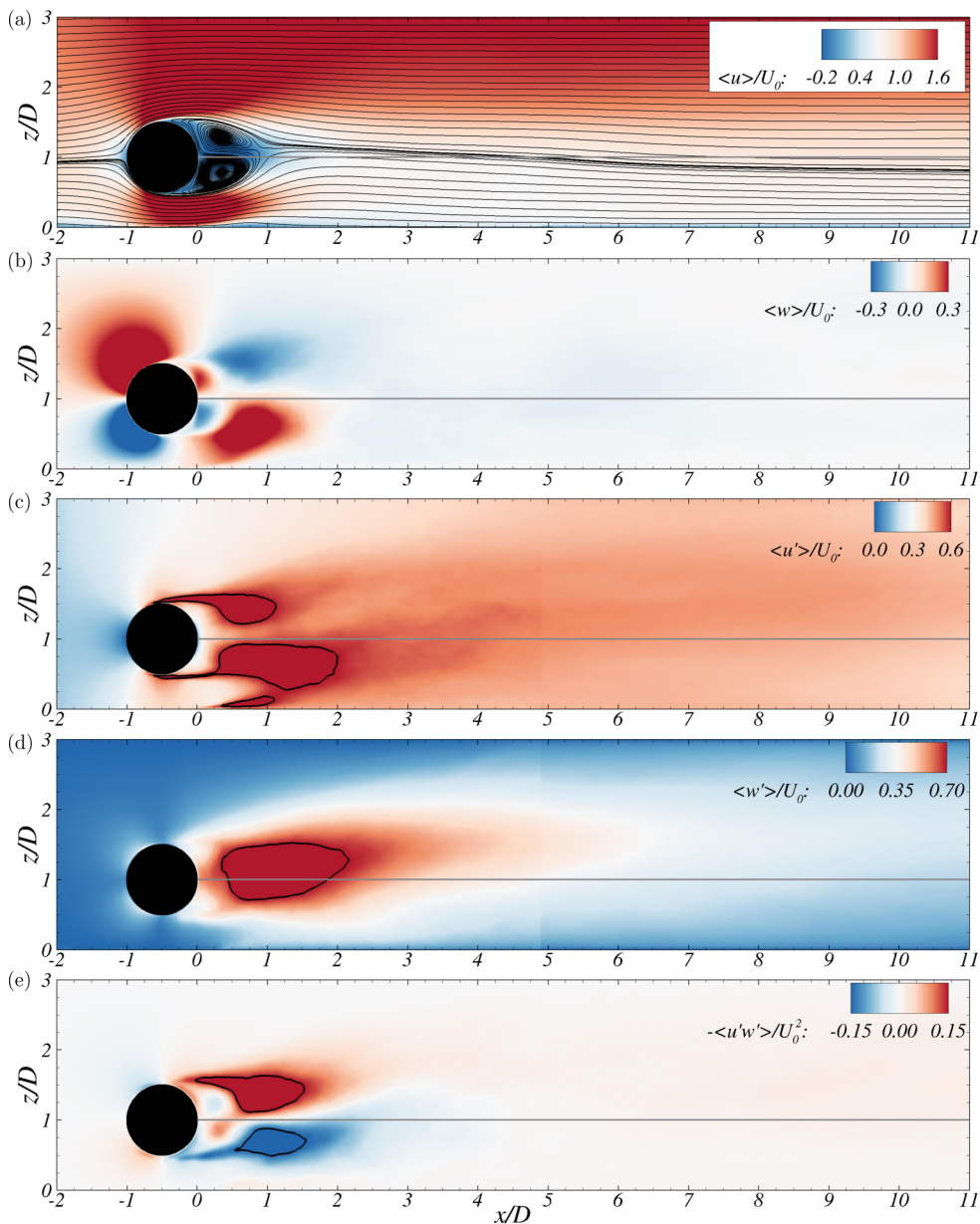


FIG. 4. Side elevation contour plots of the LES computed (a) streamwise velocity, (b) vertical velocity, (c) streamwise turbulence intensity with lines denoting  $\langle u' \rangle / U_0 = 0.6$ , (d) vertical turbulence intensity with lines denoting  $\langle w' \rangle / U_0 = 0.7$ , and (e) Reynolds shear stress with the solid lines corresponding to  $\langle u'w' \rangle / U_0^2 = \pm 0.15$ , normalized by the bulk velocity for the  $Re = 6666$  and  $G/D = 0.5$  case.

the influence of the ground effect in the time-averaged flow field is deemed small [1,2]. This can be observed from the streamlines in Fig. 4(a) which show the lower half of the wake extending over the wake center line, i.e.,  $z/D > 1$ , until a distance  $x/D = 5$ , while in the upper layer near the free-surface layer the streamlines are nearly parallel. This asymmetric flow pattern is further indicated by the distribution of the vertical velocities whose magnitude becomes notably reduced after  $x/D = 1.5$ . It is worth noting that no wall boundary layer separation upstream of the cylinder

occurs, as the Reynolds numbers of the present flow conditions are well above the threshold of  $Re = 1400$  at which such separation vanishes [16].

The examined cases are for Reynolds numbers within the subcritical cylinder flow regime in which the shear layers are laminar while the wake is fully turbulent, i.e., the present unsteady wake lies within the shear-layer transition regime identified in Williamson [13], in which shear layers remain laminar immediately after departing from the cylinders sides. As shown later in Sec. IV E, these start to become unsteady at a closer distance to the cylinder with increasing  $Re$ , due to Kelvin-Helmholtz instability. This laminar-to-turbulence transition of the turbulent structures is accompanied by the turbulent nature of the near wake enclosed to the downstream side of the cylinder. Levels of computed streamwise turbulence intensity [Fig. 4(c)] are larger than  $\langle u' \rangle / U_0 = 0.6$ , indicating that the near wake is remarkably unsteady. There is also an uneven distribution of  $\langle u' \rangle$  along the center line of the cylinder wake ( $z/D = 1$ ) with the turbulent region below this elevation extending almost twice the length than in the region higher up in the wake. Interaction between the cylinder-induced near wake and the ground can be appreciated from the distribution of high  $\langle u' \rangle$  values near the bed between  $0 < x/D < 2$  reaching values up to 0.65.

The asymmetry of the turbulent wake in the downstream direction is again depicted in the distribution of  $\langle w' \rangle$  presented in Fig. 4(d) with a well-defined area of  $\langle w' \rangle / U_0 > 0.7$  found between  $0.4 < x/D < 2.2$ . Interestingly, a larger portion of this high vertical turbulence intensity region is located above the cylinder center line,  $z/D = 1$ , while predominantly below the center line for the streamwise turbulence intensity [Fig. 4(c)]. This evidences that the ground effect renders the nature of the near wake significantly more unsteady by changing the dynamics of the vortex generation and shedding which, in consequence, leads to an asymmetric wake distribution. A similar pattern is found in the distribution of vertical Reynolds shear stress ( $\langle u'w' \rangle$ ), where higher Reynolds shear stresses values above  $z/D = 1$  result from the higher momentum exchange between the flow overtopping the cylinder with the near wake than that with the flow moving under the cylinder. Overall, the time-averaged second-order statistics ( $\langle u' \rangle$ ,  $\langle w' \rangle$ ,  $\langle u'w' \rangle$ ) indicate that until  $x/D = 2$  the wake is very turbulent, followed by a region between  $2 < x/D < 5$  over which turbulence decays and is distributed uniformly over the water depth, as the wake expands over the entire water column. Moreover, negligible differences in these time-averaged flow statistics with increasing Reynolds number are observed, as shown in Fig. 20 for the  $G/D = 0.5$  and  $Re = 13333$  case.

The main hydrodynamics developed for the case with gap ratio  $G/D$  equal to 1.0 for  $Re = 6666$  are presented in Fig. 5. Increasing the distance from the cylinder to the ground leads to the recovery of the wake symmetry, as seen in the distribution of the main velocity components  $\langle u \rangle$  and  $\langle w \rangle$ . Contours of  $\langle u' \rangle$ , which represent the streamwise fluctuations derived from the shear layers and near-wake dynamics, are again symmetric and notably different from their distribution in the  $G/D = 0.5$  case [Fig. 4(c)]. A small deviation from the center line is observed in the  $\langle w' \rangle$  contours at  $x/D = 3$ , these fluctuations being larger in the upper part of the wake owed to the logarithmic inflow velocity distribution. Similarly, the two regions of Reynolds shear stress  $\langle u'w' \rangle$  attached to the cylinders downstream face have different length, which indicate that even with  $G/D = 1.0$  the wake is not precisely as that in unbounded cylinder flows.

Figure 6 presents the vertical profiles of  $\langle u \rangle$  and  $\langle u' \rangle$  at nine locations downstream of the cylinder obtained from the experiments and the LES for the cases of  $Re = 10000$  and  $13333$  and  $G/D = 0.5$ . At the locations closest to the cylinder, i.e.,  $x/D < 1.2$ , there is a significant velocity deficit behind the cylinder. LES captures well the distribution of  $\langle u \rangle$  and  $\langle u' \rangle$  over the water depth. The slight vertical offset of the computed wake is attributed to the fact LES treats the free surface as a shear-free rigid lid while water surface waviness was present in the experiments, particularly immediately after the cylinder. Further downstream, the streamwise velocity tends to recover and approach the unperturbed log-law profile found upstream of the cylinder. Until a distance of  $x/D \approx 3$ , the profiles of  $\langle u' \rangle$  feature one peak over the cylinder top (i.e.,  $z/D > 1.5$ ) and another that is larger in magnitude at  $z/D \approx 0.5$ . Such asymmetrical distribution of  $\langle u' \rangle$  evidences the ground effect in the von Kármán street as also observed in Fig. 4(c). A more uniform distribution along the water

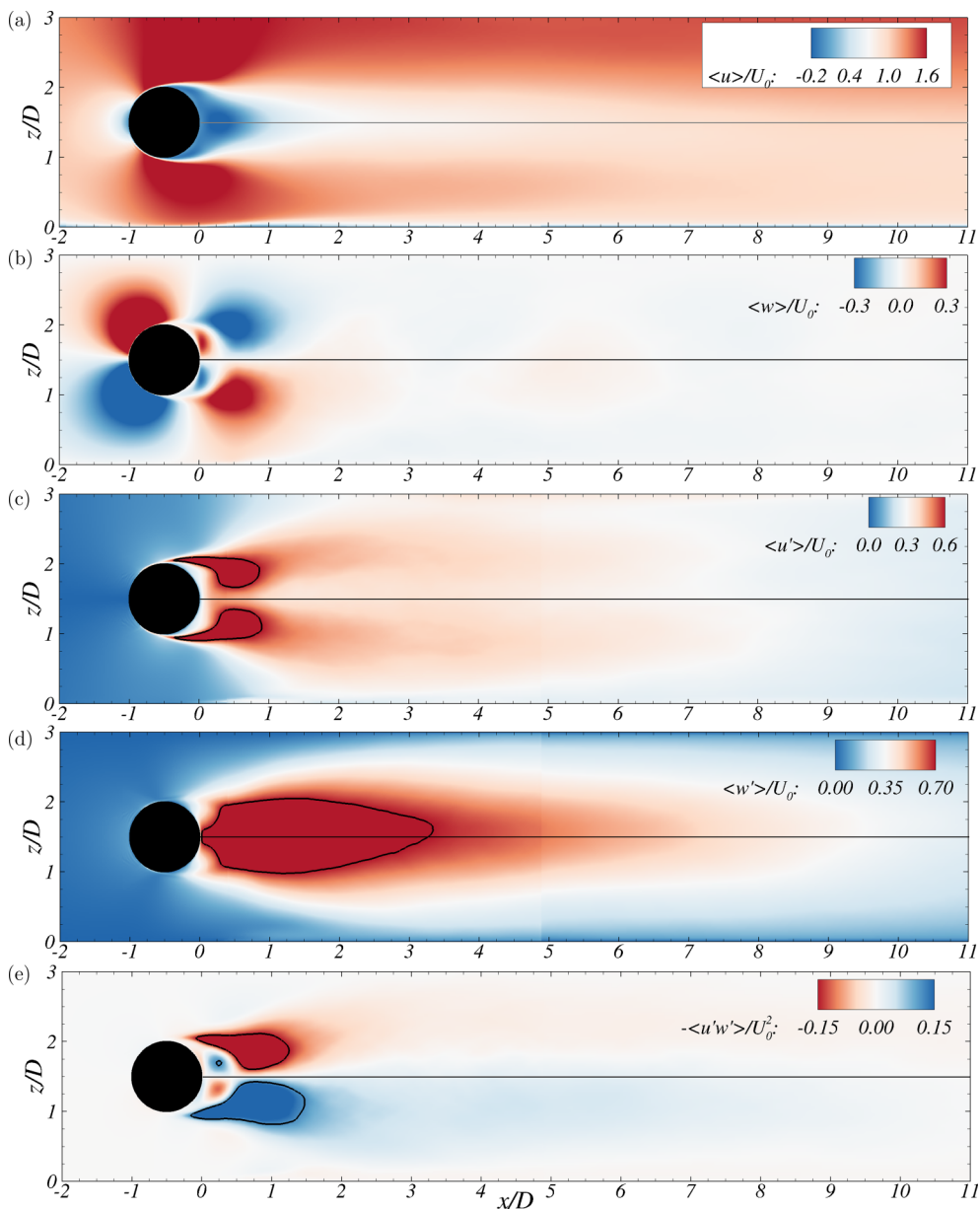


FIG. 5. Side elevation contour plots of the computed (a) streamwise velocity, (b) vertical velocity, (c) streamwise turbulence intensity with lines denoting  $\langle u' \rangle / U_0 = 0.6$ , (d) vertical turbulence intensity with lines denoting  $\langle w' \rangle / U_0 = 0.7$ , and (e) Reynolds shear stress with the solid lines corresponding to  $\langle u'w' \rangle / U_0^2 = \pm 0.15$ , normalized by the bulk velocity for the  $Re = 6666$  case and  $G/D = 1.0$ .

column is found after  $x/D = 3$ , indicating that the shed vortices have merged as explained later in Sec. IV C.

The vertical distribution of mean vertical velocity  $\langle w \rangle$  and turbulence intensity  $\langle w' \rangle$  from the experiments and LES at the channel center plane, i.e.,  $y/D = 0.0$ , is shown in Fig. 7 for the  $Re = 10000$  and  $13333$  cases and  $G/D = 0.5$ . Profiles immediately behind the cylinder show a marked upwards fluid motion below the cylinder center line resulting from the flow acceleration

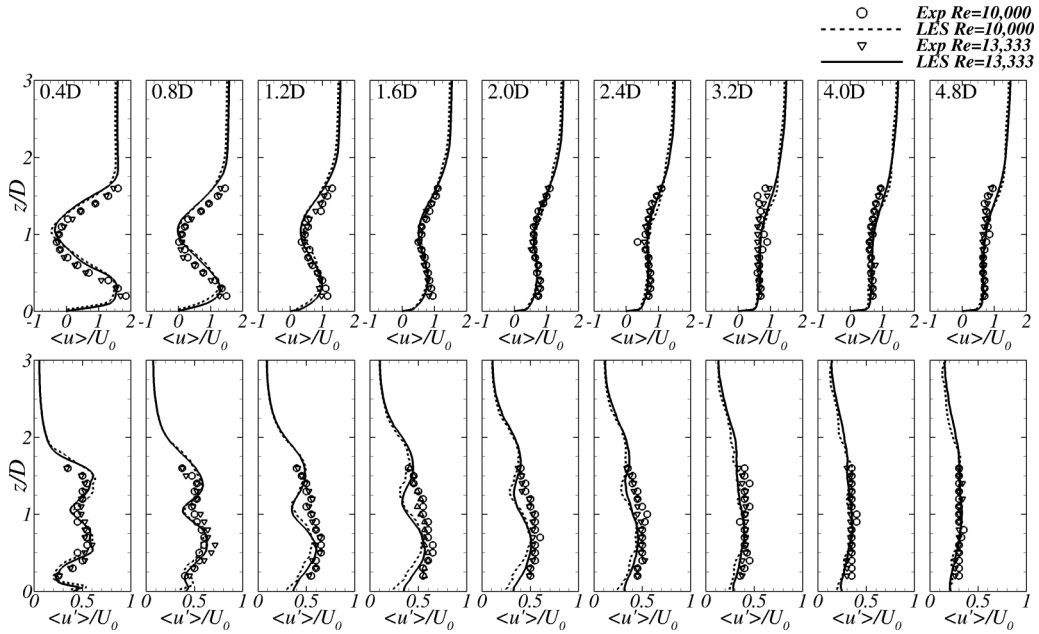


FIG. 6. Vertical profiles of mean streamwise velocity  $\langle u \rangle$  (top) and turbulence intensity  $\langle u' \rangle$  (bottom) at different locations downstream of the cylinder for the  $Re = 10000$  and  $13333$  cases and  $G/D = 0.5$ . Comparison between experimental (symbols) and LES (lines) results.

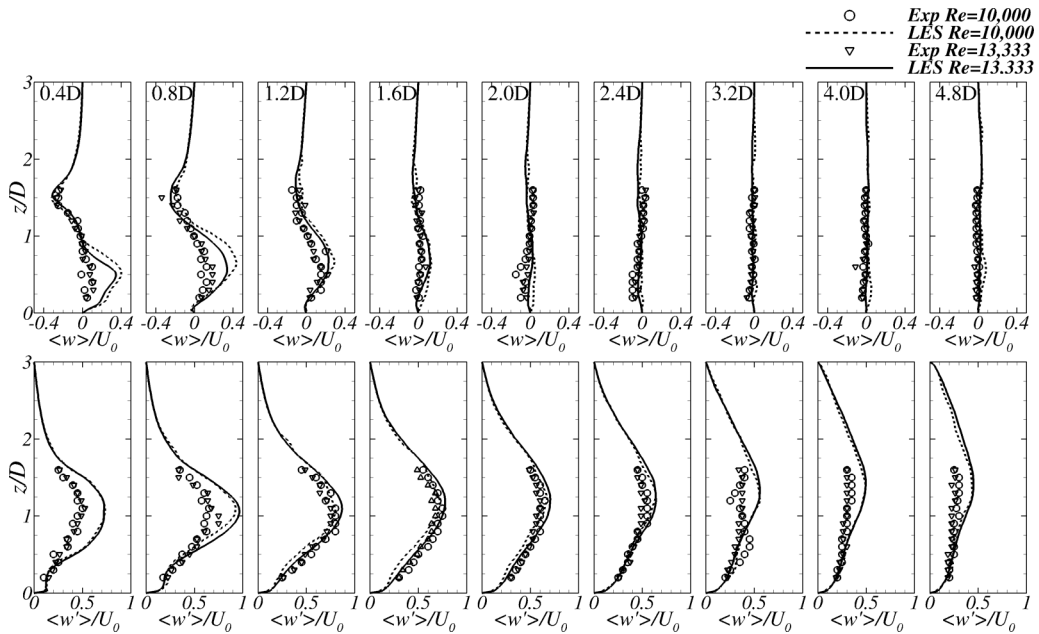


FIG. 7. Vertical profiles of mean vertical velocity  $\langle w \rangle$  (top) and turbulence intensity  $\langle w' \rangle$  (bottom) at different locations downstream of the cylinder for the  $Re = 10000$  and  $13333$  cases and  $G/D = 0.5$ . Comparison between experimental (symbols) and LES (lines) results.

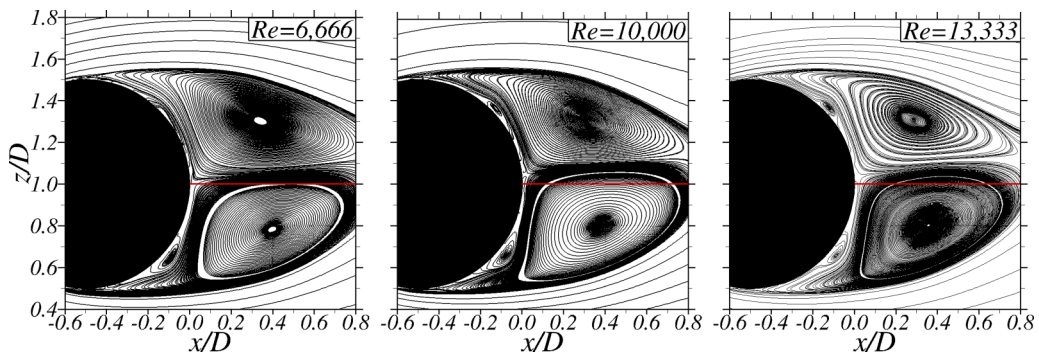


FIG. 8. Mean recirculation region computed using LES with  $G/D = 0.5$ . Red line indicates the cylinder center line at  $z/D = 1.0$ . Flow is from left to right.

through the bed-cylinder gap. Vertical turbulence intensity profiles show that near the bluff body the maxima are attained along the cylinder center line; however, further downstream the peak of  $\langle w' \rangle$  shifts toward the free surface as a result of the von Kármán vortices moving to the region of highest momentum. LES overpredicts the values of  $\langle w \rangle$  close to the bed immediately behind the cylinder while there is a good match with the experimental results above the cylinder center line ( $z/D = 1.0$ ). A similar pattern is found for  $\langle w' \rangle$  in the near wake, although LES achieves a good match with experimental results immediately behind the wake bubble ( $x/D > 1.2$ ). Overall, the normalized distribution of these mean quantities follows a very close distribution for the three cases, the remaining sources of data disparity are probably related to not modeling the free-surface deformation and the fact that inflow conditions used in the LES differed from the fully developed flow attained in the experiments which can affect the near-wake results.

### B. Recirculation region

Further insights into the asymmetric wake enclosed behind the cylinder for the different flow rates studied with  $G/D = 0.5$  are given in Fig. 8. The flow streamlines indicate that in all cases the two recirculating cells are not symmetrically distributed about the cylinder center line and are slightly shifted toward the free surface. This shift is more pronounced with increasing Reynolds number. The spatial resolution of the flow streamlines used to deduce the separation point off the cylinder sides is approximately half of the grid size. The recirculation length ( $L_{\text{rec}}/D$ ) shortens with increasing Reynolds number as presented in Table III, and its values are similar to those reported for unconfined cylinder flows [6,7]. Results also show that increasing the gap ratio decreases the recirculation length due to the change in the wake recovery dynamics [26]. Similarly, the streamwise

TABLE III. Characteristics of the recirculation area for the different cases analyzed: normalized recirculation length ( $L_{\text{rec}}/D$ ), location of the upper and lower recirculation cores ( $x^c$ ,  $z^c$ ) and upper ( $\theta^{\text{up}}$ ) and lower ( $\theta^{\text{low}}$ ) separation angles.

Re	$G/D$	$L_{\text{rec}}/D$	$x_{\text{up}}^c$	$x_{\text{low}}^c$	$z_{\text{up}}^c$	$z_{\text{low}}^c$	$\theta^{\text{up}}$ [deg]	$\theta^{\text{low}}$ [deg]
6 666	0.5	1.389	0.837	0.895	0.303	-0.218	95.7	101.3
6 666	1.0	1.118	0.760	0.747	0.252	-0.259	93.4	90.6
10 000	0.5	1.348	0.792	0.876	0.316	-0.200	92.9	97.6
10 000	1.0	1.117	0.728	0.737	0.252	-0.256	91.7	85.6
13 333	0.5	1.233	0.785	0.855	0.307	-0.198	86.6	95.7
13 333	1.0	1.066	0.741	0.697	0.246	-0.276	85.0	83.5

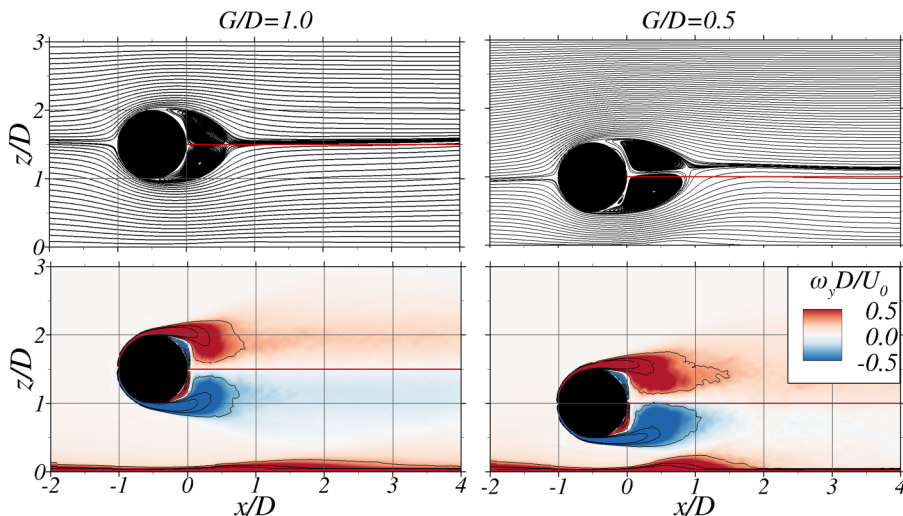


FIG. 9. Comparison of the mean recirculation region (top) and spanwise vorticity from the LES of the cylinder at  $G/D = 1.0$  (left) and  $0.5$  (right) for  $Re = 13\,333$ . Red line indicates the cylinder center line at  $z/D = 1.0$ . Flow is from left to right.

location of the upper and lower recirculation cores,  $x_{up}^c$  and  $x_{low}^c$ , is closer to the cylinder for larger Reynolds numbers, while the vertical core location,  $z_{up}^c$  and  $z_{low}^c$ , increases as a result of a larger mean wake asymmetry. For the  $G/D = 1.0$  case, the loci of both upper and lower recirculation cores are symmetric to the wake center line, the upper cell being slightly longer as shown in Table III. Flow streamlines allow the precise location at which the boundary layers separate on both upper and lower halves of the cylinder. Both separation points move upstream with increasing Reynolds number, as shown in previous studies [2], and coincide with the successive reduction of the separation angles at the upper ( $\theta^{up}$ ) and lower ( $\theta^{low}$ ) half of the cylinder, as presented in Table III. From Fig. 8, it is also observed that the locus of the upper cell is closer to the cylinder than the bottom cell as the fluid flows faster under the cylinder than over it, which is again reflected in values of  $\theta^{low}$  being larger than  $\theta^{up}$ . Interestingly, for the three flow conditions studied, two laminar separation bubbles appear enclosed between the lee-side of the cylinder and the recirculation cells.

Comparison of the impact of the proximity to the ground in the recirculation area behind the cylinder is shown in Fig. 9. For the largest gap ratio, the streamlines distribution is symmetric to the wake center line, while for  $G/D = 0.5$  the asymmetry is observed even at distances larger than  $x/D = 4$  downstream. Another representation of the time-averaged dynamics of the vortex shedding is the mean spanwise vorticity ( $\omega_y$ ) presented in Fig. 9(b). In both cylinder positions, two regions of high vorticity are developed in the shear-layer region, and this is mostly symmetric for  $G/D = 1.0$ . For the case with the cylinder impacted by the ground effect, the upper region of high vorticity extends slightly longer than the bottom one which is influenced by the ground vortex, as explained later in Sec. IV E.

### C. Centreline profiles

The distribution of the mean flow field along the cylinder center line ( $z/D = 1$ ) with increasing downstream distance from the cylinder for  $G/D = 0.5$  is shown in Fig. 10 with longitudinal profiles of mean streamwise and vertical velocities, and turbulence intensities from both the experiments and LES. Figure 10(a) shows the velocity reversal in the attached recirculation area with a peak reversal of  $-0.4U_0$ . The recirculation area ends by  $1D$  downstream of the cylinder as indicated by the positive streamwise velocity. For all cases analyzed, the streamwise momentum has nearly

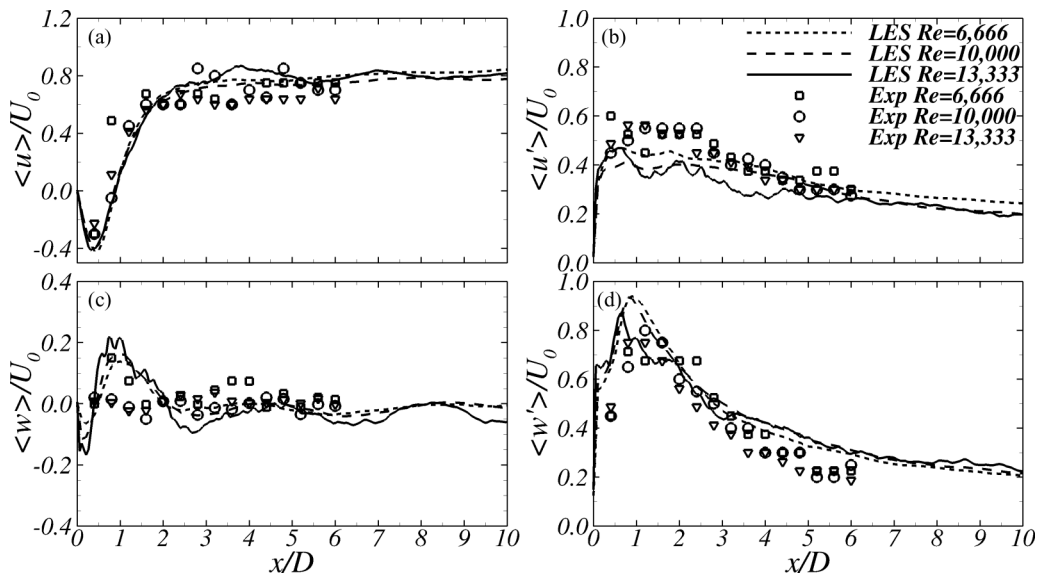


FIG. 10. Center-line profiles of normalized  $\langle u \rangle$ ,  $\langle u' \rangle$ ,  $\langle w \rangle$ , and  $\langle w' \rangle$  from experiments and LES for the three Reynolds numbers and  $G/D = 0.5$ .

recovered, i.e.,  $\langle u \rangle / U_0 \approx 0.8$ , by a downstream distance of  $3D$ , and there is a good agreement between measured data and LES. Fig. 10(b) shows that there is a similar trend in the evolution of  $\langle u' \rangle$  for cases of  $Re = 6666$  and  $10000$ , with experiments and LES data almost coinciding to a value close to  $\langle u' \rangle = 0.4U_0$  at a downstream distance of  $3D$ , after which the streamwise turbulence intensities progressively decay with increasing downstream distance. However, in the near wake the computed streamwise turbulence intensities are lower than the experiments, attributed to the lack of resolving the free surface which may lead to a slight change in the vortex generation dynamics.

Centreline plots for  $\langle w \rangle$  from Fig. 10(c) show that in the region between  $1-2D$  immediately downstream of the wake bubble, i.e., where the large-scale vortices are shed, there is a peak in positive  $\langle w \rangle$  denoting predominant upwards fluid motion. The ground effect is responsible for suppressing the symmetry in the vortex shedding mechanism compared to unbounded cylinder flows, which feature zero values of  $\langle w \rangle$  along the cylinder center line. By a downstream distance of  $2D$ , the vertical velocities decrease and by  $10D$  these are essentially zero for all three flow conditions. Regarding the distribution of vertical turbulence intensity [Fig. 10(d)] the maxima are achieved at  $x/D = 1$  for the LES and at  $x/D = 1.5$  in the experiments, which are significantly larger than those found for the streamwise turbulence intensity. Close agreement between computed and measured results is observed by a downstream distance of  $2D$  with  $\langle w' \rangle$  attaining a value of nearly  $0.7U_0$  and progressively decaying until  $0.2U_0$  further downstream.

#### D. Continuity equation terms analysis

The asymmetric near-wake recovery can be further characterised by considering the mean velocity terms in the continuity equation:

$$\frac{\partial \langle u \rangle}{\partial x} + \frac{\partial \langle v \rangle}{\partial y} + \frac{\partial \langle w \rangle}{\partial z} = 0. \quad (5)$$

In an unbounded environment these terms should be symmetric to the cylinder center line but are expected to change in the present case due to the proximity of the cylinder body to the flume bed. The term  $\partial \langle v \rangle / \partial y$  is deemed much smaller than the other two as the main flow direction is in the  $xz$

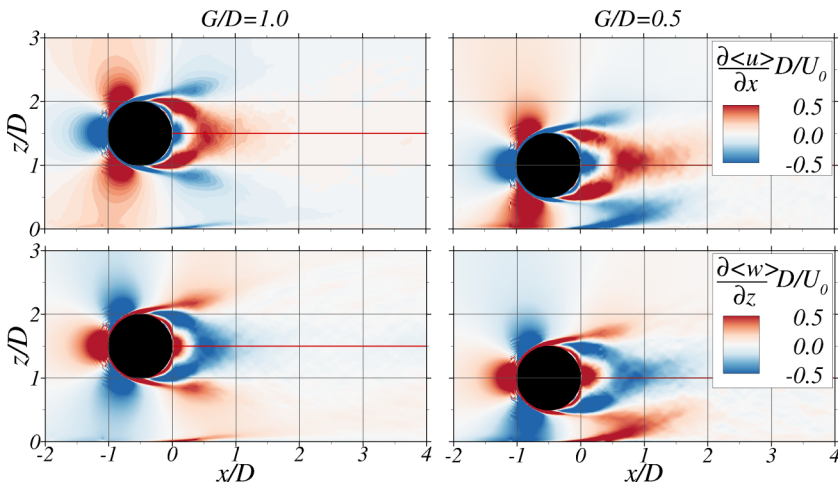


FIG. 11. Contours of the continuity equation terms for the  $Re = 13333$  case with  $G/D = 1.0$  (left) and  $0.5$  (right).

plane. Figure 11 presents the contour plots of the terms  $\partial \langle u \rangle / \partial x$  and  $\partial \langle w \rangle / \partial z$  for the  $Re = 13333$  case for both gap-to-diameter ratios. For the short gap case, the regions of highest rate-of-change of  $\langle u \rangle$  in the streamwise direction are found in the core of the near wake between  $0 < x/D < 2$  and  $0.5 < z/D < 1.5$ . For this configuration, the streamwise change of  $\langle u \rangle$  is asymmetric to the wake center line due to its proximity to the ground, while with  $G/D = 1.0$  the term  $\partial \langle u \rangle / \partial x$  is symmetric to the center line. In both cases, these regions coincide with those with the largest negative rate-of-change of  $\partial \langle w \rangle / \partial z$ , as both terms need to balance in Eq. (5). A region of negative  $\partial \langle u \rangle / \partial x$  develops over the upper shear layer until  $x/D \approx 0.5$  indicating a decrease in  $x$  velocities along the streamwise direction, irrespective of the cylinder position. However, with  $G/D = 0.5$ , in the gap between the flume's bed and cylinder such a region of  $\partial \langle u \rangle / \partial x < 0$  extends until  $x/D < 1.5$  as a result of the wake dynamics affected by the close proximity to the ground.

Upstream of the cylinder, an area of  $\partial \langle u \rangle / \partial x > 0$  is present as the approach flow accelerates on its upper and lower sides, while a reduction of  $\langle u \rangle$  is seen near the stagnation point. A reverse distribution is found for  $\partial \langle w \rangle / \partial z$  in the near wake of the cylinder. Both terms from the continuity equation show minor variations amongst the three flow discharges analyzed for both geometries analyzed, with the mass conservation [Eq. (5)] being satisfied.

### E. Instantaneous flow structures

The unsteady nature of the flow structures developed behind the cylinder are shown in Fig. 12 with contours of  $y$  vorticity at three different spanwise locations ( $y/D = 0.5, 3.0,$  and  $5.0$ ) for the case  $Re = 6666$  with  $G/D = 0.5$ , which shows the spanwise variation of the vortical structures. Shear layers are developed along the cylinder surface and separate on the lee-side featuring a laminar nature until becoming unstable due to the shear caused by the low-momentum near wake and the fast-flowing fluid over the cylinder. Following a Kelvin-Helmholtz instability, the shear layers breakdown into small vortices (or KH vortices) that are convected downstream, eventually merging with the fully turbulent near wake between  $0 < x/D < 1$ . Such flow separation is expected at these Reynolds numbers as they correspond to the subcritical regime.

The transition from the shear layers to the generation of KH vortices is non uniformly distributed across the entire spanwise length of the cylinder as observed from the spanwise-vorticity contours. Such three-dimensional variation of the shear layers' roll-up is known as intermittency that is a function of the spanwise distance [45,46]. The onset of KH instabilities developed in the upper and

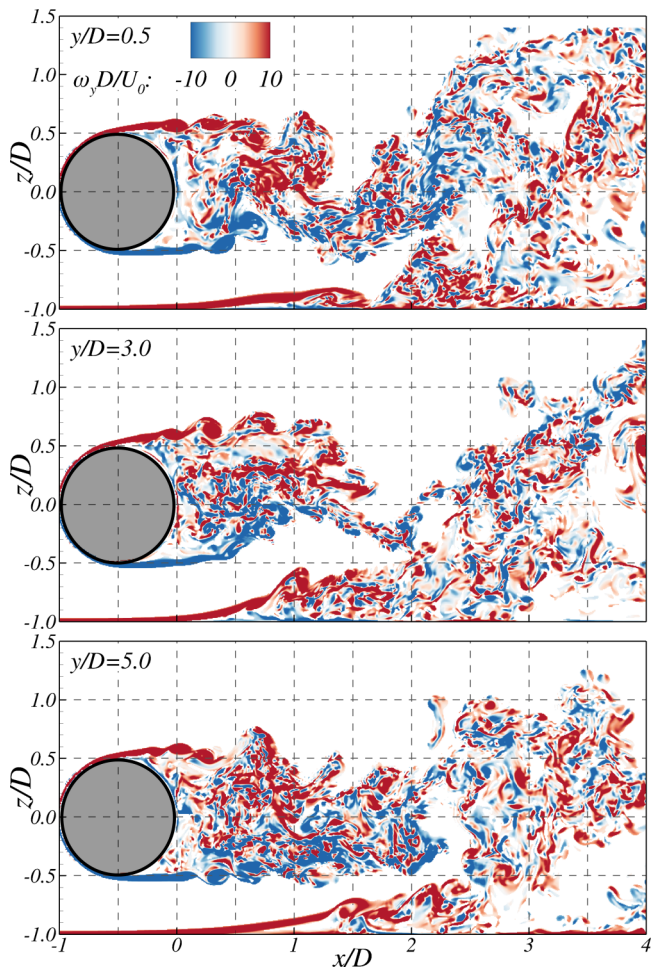


FIG. 12. Contours of normalized spanwise vorticity at three different spanwise locations across the cylinder for the  $Re = 6666$  and  $G/D = 0.5$  case. Flow is from left to right.

lower shear layers are decorrelated, i.e., there is no synchronisation in their generation, e.g., at  $y/D = 0.5$  the first roller developed from the lower shear is observed at  $x/D \approx 0.2$ , while the upper shear layer has rolled up shortly after its separation point from the cylinder transitioning to turbulent flow. Here, only the Reynolds number 6666 case is shown for brevity. Nonetheless, similar instantaneous flow patterns in the near wake are observed for all Reynolds numbers examined although there are some differences, e.g., more rapid breakdown of the shear layers with a higher Reynolds number, as indicated by the different separation angles show in Fig. 8 and the values presented in Table III.

In the region between  $1 < x/D < 2$ , the attached unstable near-wake transitions to large-scale von Kármán vortices, characteristic of the far wake behind bluff bodies. Here the proximity of the cylinder to the flume bed for the case  $G/D = 0.5$  leads to the generation of a wall shear layer and a subsequent ground vortex (GV) as depicted in Fig. 12. This region of flow separation originates from the low-pressure generated by the unsteady wake during the formation of the rollers off the lower shear layer of the cylinder. Three regions can be distinguished: a stable shear layer until  $x/D = 1$ , a separation bubble and the eventual generation of the GV. The latter eventually grows

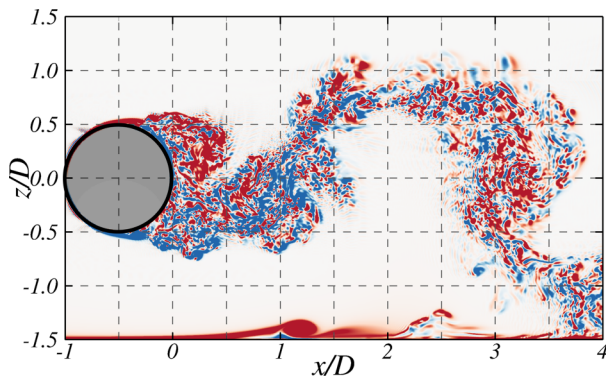


FIG. 13. Contours of normalized spanwise vorticity at a plane at  $y/D = 3.0$  for the  $Re = 13\,333$  and  $G/D = 1.0$  case. Flow is from left to right. Same color range as in Fig. 12.

and detaches, lifting off the ground and interacting with the vortical structure generated behind the cylinder, constraining the formation of the lower roller while pairing with the energetic structures, i.e., von Kármán vortices, of oppositely signed vorticity as it is convected downstream to form a single vortical structure after  $x/D > 2$ .

This complex GV-cylinder wake interaction occurs at  $G/D = 0.5$  for all three Reynolds numbers analyzed and is very similar to those found at lower  $Re$  in previous studies [3,16]. However, it is more pronounced for the highest Reynolds number case as the near wake becomes more unstable, thus leaving more space for the GV to develop. Conversely, increasing the gap ratio to 1.0 leads to a notable reduction in the instantaneous cylinder flow dynamics attributable to proximity to the bottom wall. Fig. 13 shows spanwise vorticity contours for  $Re = 13\,333$  at  $y/D = 3.0$  in which the GV appears but has no effect on the generation of the von Kármán vortices immediately behind the cylinder. Increasing the gap ratio reduces flow acceleration close to the ground, which leads to a more uniform GV in the spanwise direction, contrary to its changing shape for  $G/D = 0.5$  shown in Fig. 12. Further details on the generation of the GV are discussed in Sec. V.

This ground-effect phenomenon has previously been observed in experimental studies [1,2,16,21] and motivated computational analyses using Reynolds averaged Navier-Stokes [17], detached-eddy simulation [26], LES [3], and DNS in the laminar regime [18,19]. The gap-to-diameter ratio ( $G/D$ ) setup of 0.5 corresponds to the intermediate gap regime which relates the influence of the ground effect on the cylinder's near-wake structure and more specifically regulates whether large-scale von Kármán vortices are shed or not [1,2]. For  $G/D = 0.5$ , the ground influence is relatively small allowing the large-scale vortices to be shed but their active interaction with each other, as shown in Fig. 12, is in contrast to unbounded cylinder flows.

Prasad and Williamson [45] described two main of intermittent secondary instabilities developed in the shear layers and roll-up vortices in addition to the classic primary instability which is the shedding of von Kármán vortices. Two main secondary instabilities modes can be found in the cylinder flow in the subcritical regime: mode A resulting from the vortex dislocations in narrow spatial regions, also referred to as “3D instability,” and mode B as an oblique convection of the KH vortices during their early shedding, i.e., before rolling up to von Kármán vortices, known as “quasi-2D instability” [47]. Both modes appear in the present cases. Figure 14 shows the top view of isosurfaces of normalized  $Q$  criterion [48] ( $Q^* = QD^2/U_0^2 = 21$ ) colored with relative elevation  $z/D$  for the  $Re = 13\,333$  case and  $G/D = 0.5$ .

The Kelvin-Helmholtz instability developed by the transition of shear layers coming off the edge of the cylinder to smaller rollers is shown to occur closer to the cylinder's wall for the  $Re = 13\,333$  case than the  $Re = 6\,666$  case. Thereafter, in the near-wake region spanwise rollers

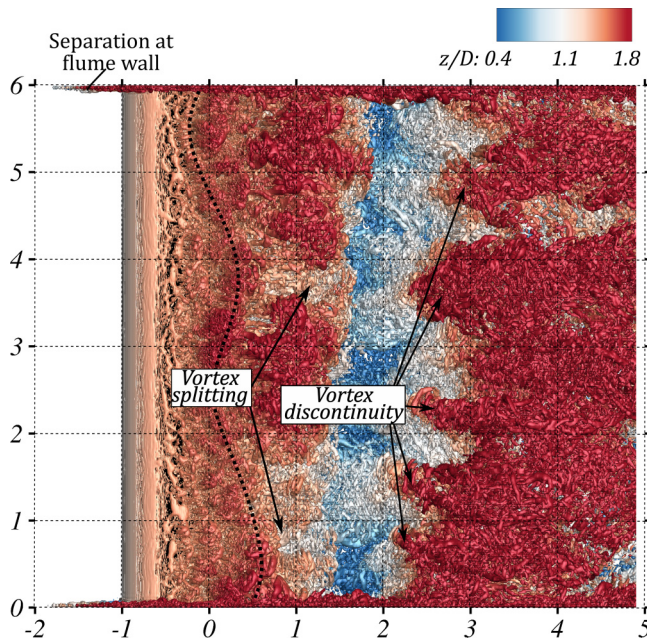


FIG. 14. Top view of isosurfaces of  $Q$  criterion ( $Q^* = QD^2/U_0^2 = 21$ ) colored by the relative elevation  $z/D$  for the  $Re = 13\,333$  case and  $G/D = 0.5$ . Arrows indicate the location of the vortex discontinuities. Flow is from left to right.

are formed with an undulating shape instead of being parallel to the cylinder edge (as marked with dotted line in Fig. 14), which exhibits a wavelength  $\lambda$  of approx.  $\pi D/2$ , in agreement with the findings from Braza *et al.* [49] who quantified that this wavelength can vary from  $3.0\text{--}4.5D$ . Interestingly, vortex discontinuities caused by the large-scale von Kármán vortices are irregularly distributed across the whole spanwise length, as mode A instabilities [47]. There is some correlation between the undulated spanwise roller and vortices dislocations [13], as those dislocations found at  $y/D \approx 3.8$  or  $1.0$  are located further downstream in-line with low-momentum regions developed in the downstream roller at  $x/D \approx 1$ . At the time instance shown in Fig. 14, the large-scale structures at elevations  $z/D > 1$  found between  $3 < x/D < 5$  are convected downstream in an oblique manner, i.e., with an angle relative to the cylinder edge. This is a well-known feature of the far wake in cylinder flows [13] and interestingly occurs in the present case even though the flow is laterally constrained by the flume sidewalls, which also induce flow separation although its effect on the main wake structure is thought to be minimal.

Figure 15 gives further insight into the instantaneous vortex shedding for the  $Re = 13\,333$  and  $G/D = 0.5$  case with isosurfaces of pressure fluctuation ( $p' = p - \langle p \rangle$ ) and  $Q$ -criterion at time instants every  $T/6$ , where  $T = 1/f_p$ ,  $T$  and  $f_p$  being the vortex shedding period and frequency, respectively. Figure 15(a) depicts the roller  $R_1$  coming off the upper surface of the cylinder is somewhat coherent over the spanwise direction as a unique structure and features an undulating or wavy shape and sheds in a slightly oblique manner as mode B instability. Shortly after, at  $2T/6$  [Fig. 15(b)], at  $x/D = 1.0$  the roller  $R_1$  develops a discontinuity,  $D_1$ , and is divided into main two finite spanwise long rollers that are convected downstream with the mean flow and whose size increases at the next time instant  $3T/6$ . This sequence is analogous to the vortex splitting identified in Fig. 14. At  $x/D = 2$  [Fig. 15(d)], the rollers start to feature smaller scale, localized instabilities as a result of their interaction with the turbulent flow going over the cylinder, which is linked to mode A instabilities. These small scale vortices result from the change in vorticity [49], which was observed during experiments [50], and grow in size during their downstream convection, as seen in Figs. 15(e)

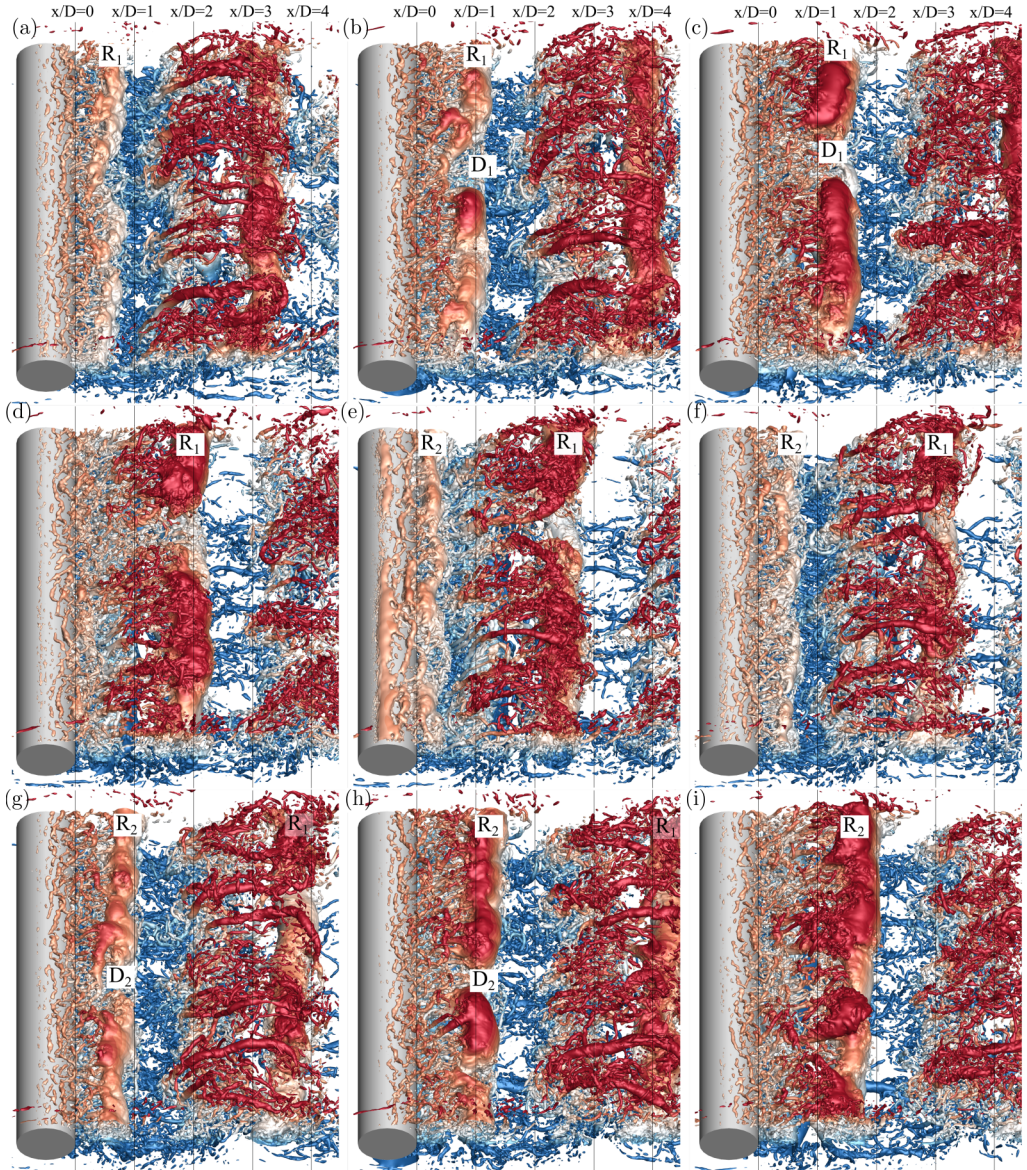


FIG. 15. Snapshots of isosurfaces of instantaneous pressure fluctuation,  $p'$ , and  $Q$  criterion colored with vertical elevation (see contour label in Fig. 14) for the  $Re = 13\,333$  and  $G/D = 0.5$  case. An interval of  $T/6$ , with  $T$  being the vortex shedding period, is kept between snapshots. Flow is from left to right.

and 15(f). Note that despite these turbulent structures originating with the roller, they appear to be connected to the vortical structures shed from the bottom half of the cylinder, as shown in Fig. 12 in the far-wake region at  $x/D > 2$ . Instantaneous flow structures in Figs. 15(g), 15(h) and 15(i) capture the formation of a new roller,  $R_2$ , which is again shed obliquely to the transverse direction similarly to previous experimental observations [45]. Interestingly, this roller again features a dislocation  $D_2$  but at a different spanwise location to that shown in Fig. 15(a), identifying the intermittent nature of the shear layer breakdown.

TABLE IV. Values of time-averaged drag ( $\overline{C_D}$ ) and lift ( $\overline{C_L}$ ) coefficients and their root-mean square, peak frequencies ( $f_p$ ), and Strouhal number (St) obtained in the experiments and LES.

Re	$G/D$	$\overline{C_D}$	rms( $C_D$ )	$\overline{C_L}$	rms( $C_L$ )	$f_p$ (LES) [ $s^{-1}$ ]	$f_p$ (Exp) [ $s^{-1}$ ]	St (LES)	St (Exp)
6 666	0.5	0.443	0.062	0.014	0.142	0.819	0.85	0.307	0.32
6 666	1.0	0.447	0.059	-0.019	0.059	0.801	-	0.300	-
10 000	0.5	0.414	0.062	0.015	0.155	1.105	1.21	0.276	0.30
10 000	1.0	0.441	0.054	-0.015	0.064	1.087	-	0.271	-
13 333	0.5	0.400	0.059	0.017	0.158	1.490	1.61	0.279	0.30
13 333	1.0	0.424	0.053	-0.014	0.064	1.372	-	0.257	-

### F. Dominant shedding frequency and hydrodynamic coefficients

The hydrodynamic forces generated on the cylinder are impacted by the asymmetric flow field developed around the cylinder owing to both its proximity to the bed and the upstream velocity logarithmic distribution. The cylinder forces are directly calculated from the immersed boundary method [36] in the horizontal and vertical directions,  $F_x$  and  $F_z$ , respectively, and are used to calculate the drag ( $C_D$ ) and lift ( $C_L$ ) coefficients given by

$$C_D = \frac{F_x}{1/2\rho AU_0^2}, \quad (6)$$

$$C_L = \frac{F_y}{1/2\rho AU_0^2}, \quad (7)$$

where  $\rho$  is the fluid density and  $A$  is the cylinder's cross-sectional area. Values of the time-averaged hydrodynamic coefficients and their root-mean-square (rms) values are presented in Table IV. The drag coefficient decreases with increasing Reynolds number, with values considerably lower than those found in unbounded cylinder flows due to the proximity of the cylinder to the bed [21,23], and the shallow flow conditions that increase the relative flow blockage of the cylinder. Time-averaged fluctuations of  $C_D$  for  $G/D = 0.5$  are similar for the  $Re = 6\,666$  and  $10\,000$  cases but decrease for the highest Reynolds number case ( $Re = 13\,333$ ), the same trend is present for  $G/D = 1.0$ . The ground effect is responsible for the upwards force with time-averaged  $C_L$  values ranging from 0.014–0.017 for  $G/D = 0.5$ , while similar  $\overline{C_L}$  magnitudes are present for  $G/D = 1.0$  as the force now acts in a downward direction. This is a consequence of the cylinder being immersed in the boundary-layer inflow, leading to a higher momentum flowing over the cylinder than beneath it [22]. The time-averaged fluctuations of the  $C_L$  are more than double the magnitude for the  $G/D = 0.5$  than for the  $G/D = 1.0$  due to the ground effect. For both gap ratio cases, the rms( $C_L$ ) values increase with increasing Reynolds number.

Figure 16 presents the power spectral distribution (PSD) of the vertical forces ( $F_z$ ) experienced by the cylinder under the flow conditions considered with gap ratios 1.0 and 0.5. For each geometry configuration, energy peaks collapse into Strouhal numbers ( $St = f_p D/U_0$ ) between 0.257 and 0.307, summarized in Table IV, with values for  $G/D = 1.0$  constantly smaller than those with a narrower gap ratio [24]. In the former configuration, the St are closer to those attained in unbounded cylinder flows, i.e.,  $St \approx 0.21$  [15], due to a reduced influence of proximity to the wall, although these remain slightly higher due to effects from the confined domain. These distinct energy peak are observed at the vortex shedding peak frequency ( $f_p$ ), which becomes higher with increasing Reynolds number as shown in Table IV. Harmonics of these frequencies observed at  $2f_p$  and  $3f_p$  are more pronounced in the configuration with the cylinder closer to the ground specially for the  $Re = 13\,333$  case. Experimental Strouhal values presented in Table IV were obtained from the PSD of the time-history of vertical velocities at the sampling point located at  $x/D = 6$ ,  $z/D = 1.5$

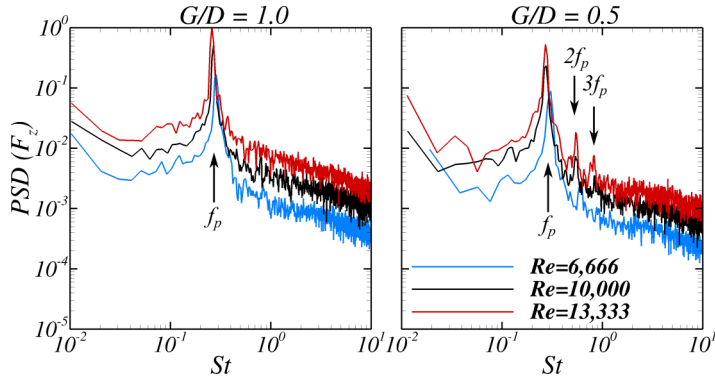


FIG. 16. Spectral energy distribution of the vertical forces ( $F_z$ ) in the cylinder computed from the LES for the three Reynolds number cases studied with gap ratios 1.0 (left) and 0.5 (right).

for  $G/D = 0.5$  and these are very close to the values from the simulations. These experimental and LES-modelled results show a slight decline in Strouhal number with increasing Reynolds number which has been observed in lower Reynolds number studies [3,16]. Furthermore, previous experimental tests reported increases in  $St$  as the  $G/D$  ratio decreased with values ranging between 0.18–0.28 with  $G/D = 0.5$  although for lower Reynolds numbers [16,21,24]. It should be noted that the logarithmic distribution of the approaching flow also affects the values of the hydrodynamic forces even for  $G/D = 1.0$  [22,23], which also explains the present  $St$  values and hydrodynamic coefficients.

## V. DISCUSSION ON THE GENERATION OF THE GROUND VORTEX

To give new insights into the ground-vortex formation and its lift up, the main interactions observed in the wake in cylinder flows in proximity of a solid wall with  $G/D = 0.5$  are summarized in Fig. 17, based on the mean and instantaneous wake distribution shown in Figs. 9(d) and 12, respectively. As the flow approaches the cylinder, it accelerates over its upper and lower sides. For small gap-to-diameter ratios, e.g.,  $G/D = 0.5$ , the flow going under the cylinder is accelerated akin to a jet-flow as a result from an adverse pressure gradient, which is larger over the region between the bed and the cylinder's underside [51]. This is supported by the distribution of  $\partial \langle u \rangle / \partial x$  in Fig. 11.

Upon passing the cylinder's underside, there is a favorable pressure gradient and the flow is able to expand vertically [15]. In this region the velocity profile is influenced by the solid cylinder and bottom walls, which induce the flow to exhibit a parabolic velocity profile [52]. Hence, the gradient

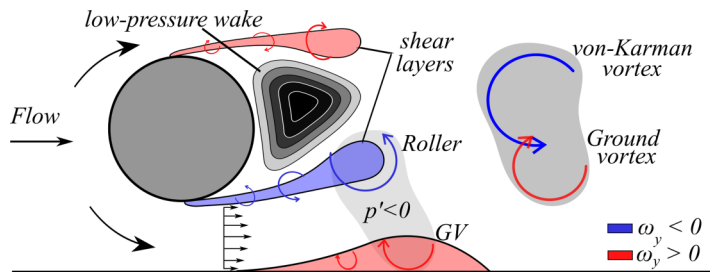


FIG. 17. Schematic of the mechanisms responsible for the appearance and progression of the ground vortex for small gap-to-diameter ratios.

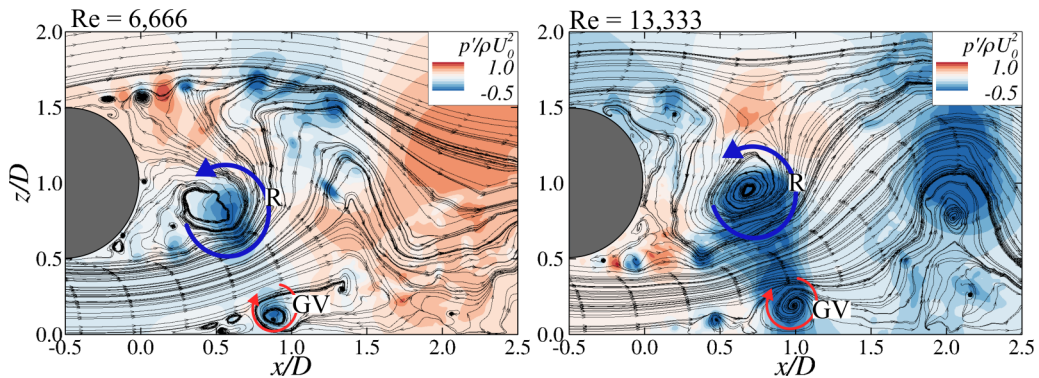


FIG. 18. Contours of normalized pressure fluctuation,  $p'/\rho U_0^2$ , with flow streamlines at a  $xz$  plane at  $y/D = 4$  for cases with  $Re = 6\,666$  (left) and  $13\,333$  (right) with  $G/D = 0.5$ .

$\partial\langle u \rangle/\partial z$  is positive near the bottom and negative in the cylinder's lower shear layer (Fig. 11). The generation of the bottom shear layer due to this velocity gradient can be well-explained by the definition of spanwise vorticity:

$$\omega_y = \frac{\partial u}{\partial z} - \frac{\partial w}{\partial x} \quad (8)$$

In the contribution to the generation of  $\omega_y$ , the term  $\partial w/\partial x$  is smaller than  $\partial u/\partial z$ , thus the vorticity field near the bottom wall is nearly proportional to the vertical gradient of streamwise velocities of positive sign, as seen in Fig. 9 d. As observed in Fig. 12, there is a region of high-vorticity attached to the bottom boundary identifying the bottom shear layer that starts to separate, i.e., increase its thickness, after surpassing the cylinder's lee side at  $x/D = 0$ , as a result of the favorable pressure gradient [15,53]. This explains that, when the bottom boundary moves [1,26] or approach flow boundary layer thickness is relatively small [53], the bottom shear layer is either attenuated or not formed due to reduced velocity gradients.

To provide further understanding of the bottom shear layer transition and interaction with the cylinder's wake, Fig. 18 presents contours of pressure fluctuation,  $p'$ , together with isolines of spanwise vorticity and flow streamlines at an  $xz$ -plane at  $y/D = 4$  for cases with  $Re = 6\,666$  and  $13\,333$  with  $G/D = 0.5$ . The flow streamlines allow to visualise the onset of a separation bubble in the bottom shear layer that rolls up, growing in size further downstream. At  $x/D = 1.0$  for both  $Re$  cases, this bubble eventually becomes large enough to generate the GV, as also depicted in Fig. 12(a). The cylinder's shear layer becomes unstable rapidly after separation with Kelvin-Helmholtz or roller structures being formed and growing in size with increasing distance downstream.

In the area occupied by the roller ( $R$ ) the values of  $p'$  are negative, where this instantaneous pressure field responsible for the quick GV liftoff, which also exhibits negative values of pressure fluctuation. This R-GV coupling is observed for both Reynolds numbers, while it is obvious in the  $Re = 13\,333$ . The mechanisms driving the near-wall flow transition, separation and instabilities is somewhat similar to those in flows over flat plate under adverse pressure gradient boundary layers but, in this case, the cylinder-shed vortical structures trigger suction areas, i.e., of negative pressure, causing the liftoff of the GV to occur relatively close to the cylinder. These observations agree very well with experimental visualisations from Bearman and Zdravkovich [15] and Grass *et al.* [53]. Finally, it is worth to mention that the GV has a clockwise rotation while the cylinder's shear layer rollers have an opposite rotational direction. Thus, once both structures merge and are shed, they form the von Kármán vortex that is convected downstream with the flow, as observed at  $x/D = 2.0$

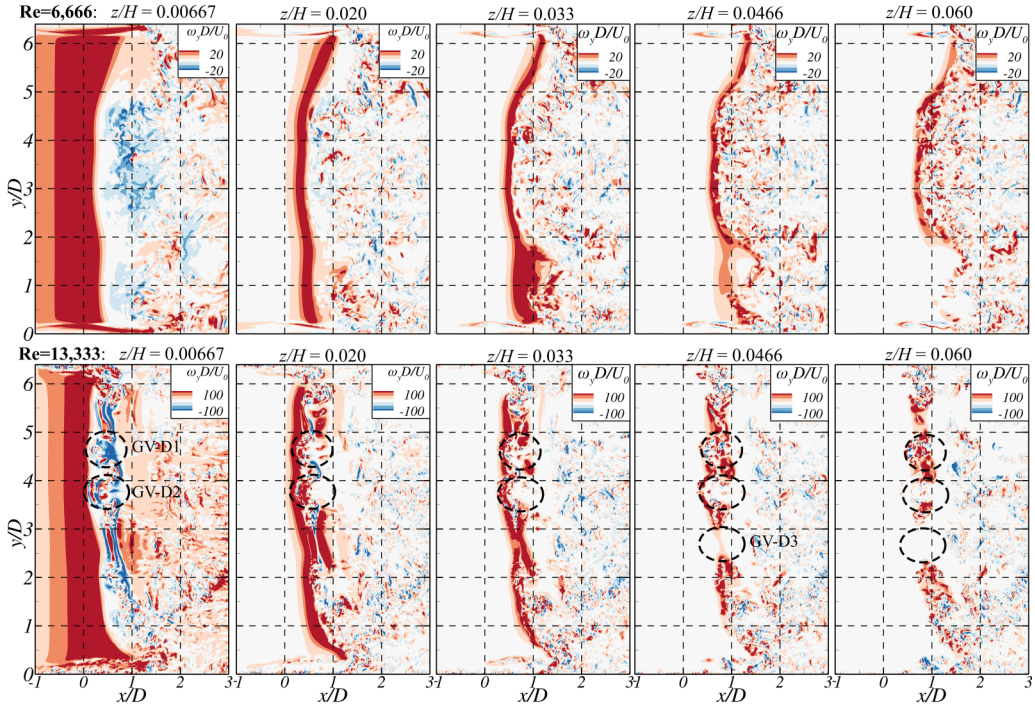


FIG. 19. Contours of spanwise vorticity at elevations  $z/H = 0.00667, 0.020, 0.033, 0.0466,$  and  $0.060$  for the cases with  $Re = 6666$  (top) and  $13333$  (bottom), and  $G/D = 0.5$ .

for the  $Re = 13333$  case, but whose expected clear counterclockwise motion is damped as result of the GV.

To better explain the detachment of the bottom shear layer off the bottom wall, Fig. 19 presents contours of spanwise vorticity at five horizontal planes at elevations  $z/H$  in the range of  $0.00667-0.060$  for  $Re = 6666$  and  $13333$  with  $G/D = 0.5$ . At the plane closest to the bottom, it is seen that the transition from the wall shear layer to the separated bubble is accomplished after  $x/D = 0$ , being more subtle for the lower  $Re$ . However, it is appreciated that the location of the transition point is heterogeneous in the spanwise direction, resulting from its intermittent motion upstream and downstream analogously to the cylinder's shear layer. It is also observed that the lateral walls induce flow separation and hence play a role in the transition of the bottom laminar shear layer to the GV formation at the ends of the domain.

Comparing the vorticity distribution for both  $Re$ , it is clear that in this near-wall region the flow separation phenomena depends on the Reynolds number. At  $Re = 13333$ , three vortex dislocations are developed, similar to those mode A instabilities found in the cylinder shear layers, with two of them,  $GV-D1$  and  $D2$ , already found near the bottom wall at  $z/H = 0.00667$  while  $GV-D3$  is observed at elevations above  $z/H = 0.0466$ . Figure 19 allows to observe that the GV, at an elevation  $z/H = 0.060$  for  $Re = 6666$ , features some spatial coherence as a long roller of high-vorticity spanning between  $2 < y/D < 5$  at  $x/D \approx 0.5$ , while for the higher Reynolds number discontinuities in the GV are observed at  $z/H = 0.0466$ .

For cases with  $G/D = 1.0$  the mechanisms responsible for connecting and merging the R and GV are almost negligible as seen in Fig. 13. Increasing the distance between the cylinder and the wall reduces the negative pressure fluctuations and their impact on the roller R interference with the GV formation and subsequent liftoff. Planviews of spanwise vorticity near the bed show that the

GV is fairly uniform across the domain length (not shown here for brevity). The bottom wall affects the far wake for the larger gap ratio in that the von Kármán vortices impingement on the ground constrains their vertical expansion. Hence, the near-wake dynamics developed behind the cylinder with  $G/D = 1.0$  are similar to those in unconfined cylinder flows, while the far wake can slightly differ due to the limited freedom of the large-scale vortices to move vertically in their downstream convection.

## VI. CONCLUSIONS

The nature of the turbulent wake behind a circular cylinder in close proximity to a solid boundary have been investigated using a combined experimental and large-eddy simulation study for Reynolds numbers in the range 6 666 to 13 333 with gap-to-diameter ratios of 0.5 and 1.0. The LES results agreed well with the experimental measurements for the time-averaged flow quantities and captured the streamwise velocity, its fluctuation in the recirculation bubble, and the upward flow motion. The presence of a narrow gap between the wall and cylinder, at a ratio of 0.5, significantly influenced the dynamics of the vortex generation and shedding which, in consequence, led to an increasingly pronounced asymmetric wake distribution with increasing Reynolds number. The boundary layer separation points on both the upper and lower halves of the cylinder move upstream with increasing Reynolds number, which is consistent with previous studies. Likewise, the enclosed recirculation bubble, was found to be slightly asymmetric by being larger in its lower part and decreasing in longitudinal extent with increasing Reynolds number consistently with cylinder-wake flows. This impact on the wake asymmetry reduced for cases with gap ratio of 1.0. From the continuity equation, the rate of change of the mean velocity terms further characterised the asymmetric near wake in the cases with the cylinder close to the ground, whose distribution was similar for the three Reynolds numbers.

The Kelvin-Helmholtz instabilities developed in the upper and lower shear layers were shown to be decoupled in that these shear layers followed a laminar-to-turbulent transition at different downstream distances. A more rapid breakdown of the shear layers occurred for the  $Re = 13\,333$  case than the  $Re = 6\,666$  case. In the near-wake region spanwise rollers were formed with an undulating pattern instead of being parallel to the cylinder edge, which was linked to the appearance of vortex dislocations. The ground vortex formed as a result of the lower vortex inducing a difference in pressure near the bottom wall which allowed the former structure to lift off the ground and merge with the von Kármán vortices to form a single vortical structure. This phenomenon was present for all three Reynolds numbers examined for the gap ratio of 0.5, and became more pronounced for the highest Reynolds number case as the near wake became more unstable closer to the cylinder.

Spectral analysis revealed Strouhal numbers varied between 0.28–0.32 for the gap ratio of 0.5 for both the experiments and LES while varied in the range of 0.25–0.30 for the gap ratio of 1.0. For all these scenarios, the Strouhal numbers remain higher than the value of 0.21 commonly found for unbounded cylinder flows owing to changes in the vortex shedding dynamics from the ground effect. In this line, drag coefficients increased when the gap between the cylinder and the ground was greater while remaining lower than those for unbounded cylinder flows. An upwards force was present on the cylinder for the gap ratio of 0.5, due to the proximity to the bottom boundary, while a mean vertical downforce was present for the case with larger gap ratio owed to the boundary layer flow carrying more momentum over the cylinder than below it.

## ACKNOWLEDGMENTS

The authors acknowledge the support of the Supercomputing Wales project, which is part-funded by the European Regional Development Fund (ERDF) via the Welsh Government. The authors would like to thank the anonymous reviewers for their suggested improvements and helpful comments.

**APPENDIX: TIME-AVERAGED FLOW HYDRODYNAMICS  
FOR THE  $Re = 13333$  AND  $G/D = 0.5$  CASE**

The influence of the Reynolds number in the wake behind the cylinder in proximity to the wall with  $G/D = 0.5$  is presented in Fig. 20 for  $Re = 13333$ .

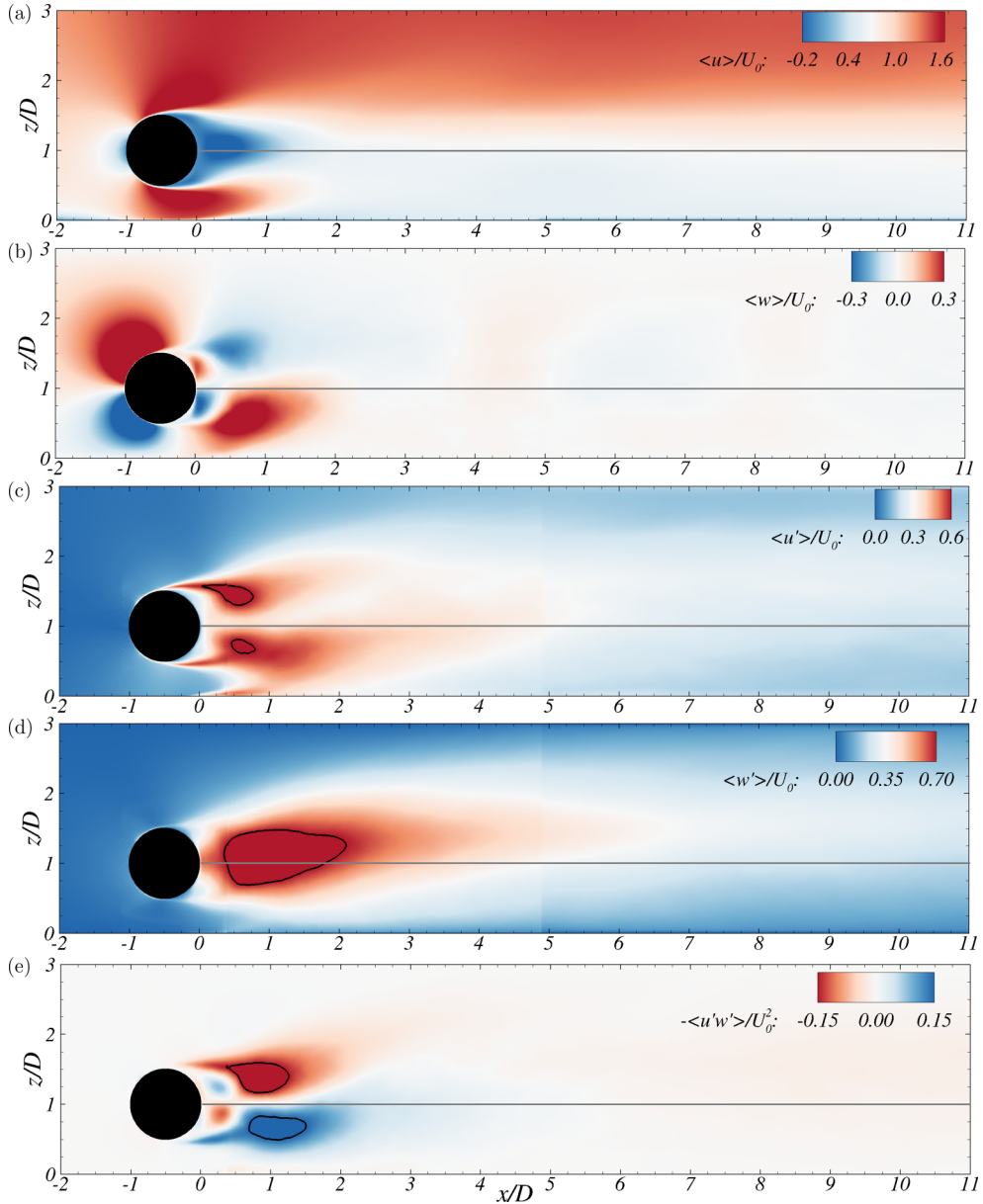


FIG. 20. Side elevation contour plots of the LES computed (a) streamwise velocity, (b) vertical velocity, (c) streamwise turbulence intensity with lines denoting  $\langle u' \rangle / U_0 = 0.6$ , (d) vertical turbulence intensity with lines denoting  $\langle w' \rangle / U_0 = 0.7$ , and (e) Reynolds shear stress with the solid lines corresponding to  $\langle u'w' \rangle / U_0^2 = \pm 0.1$ , normalized by the bulk velocity for the  $Re = 13333$  and  $G/D = 0.5$  case.

- 
- [1] T. Nishino, G. T. Roberts, and X. Zhang, Vortex shedding from a circular cylinder near a moving ground, *Phys. Fluids* **19**, 025103 (2007).
- [2] A. Oner, M. Kirkgoz, and M. Akoz, Interaction of a current with a circular cylinder near a rigid bed, *Ocean Eng.* **35**, 1492 (2008).
- [3] S. Sankar and S. Sankar, Vortex dynamics of a cylinder wake in proximity to a wall, *J. Fluids Struct.* **26**, 19 (2010).
- [4] M. Unal and D. Rockwell, On vortex shedding from a cylinder: Part 1. The initial instability, *J. Fluid Mech.* **190**, 491 (1988).
- [5] C. Chyu, J. Lin, J. Sheridan, and D. Rockwell, Karman vortex formation from a cylinder: Role of phase-locked Kelvin-Helmholtz vortices, *Phys. Fluids* **7**, 2288 (1995).
- [6] O. Lehmkuhl, I. Rodriguez, R. Borrell, and A. Oliva, Low-frequency unsteadiness in the vortex formation region of a circular cylinder, *Phys. Fluids* **25**, 085109 (2013).
- [7] D. Aljure, O. Lehmkuhl, I. Rodriguez, and A. Oliva, Three dimensionality in the wake of the flow around a circular cylinder at Reynolds number 5000, *Comput. Fluids* **147**, 102 (2017).
- [8] A. Prasad and C. H. Williamson, The instability of the separated shear layer from a bluff body, *Phys. Fluids* **8**, 1347 (1996).
- [9] C. Norberg, An experimental investigation of the flow around a circular cylinder: Influence of aspect ratio, *J. Fluid Mech.* **258**, 287 (1994).
- [10] C. Wieselsberger, Neuere feststellungen uber die gesetze des flussigkeits und luftwiderstands, *Phys. Z.* **22**, 321 (1921).
- [11] A. Roshko, Experiments on the flow past a circular cylinder at very high Reynolds number, *J. Fluid Mech.* **10**, 345 (1961).
- [12] O. Lehmkuhl, I. Rodriguez, R. Borrell, J. Chiva, and A. Oliva, Unsteady forces on a circular cylinder at critical Reynolds numbers, *Phys. Fluids* **26**, 125110 (2014).
- [13] C. Williamson, Vortex dynamics in the cylinder wake, *Annu. Rev. Fluid. Mech* **28**, 477 (1996).
- [14] D. Sumner, Flow above the free end of a surface-mounted finite-height circular cylinder: A review, *J. Fluids Struct.* **43**, 41 (2013).
- [15] P. Bearman and M. Zdravkovich, Flow around a circular cylinder near a plane boundary, *J. Fluid Mech.* **89**, 33 (1978).
- [16] S. Price, D. Sumner, J. Smith, K. Leong, and M. Paidussis, Flow visualisation around a circular cylinder near to a plane wall, *J. Fluids Struct.* **16**, 175 (2002).
- [17] M. Kirkgoz, A. Oner, and M. Akoz, Numerical modeling of interaction of a current with a circular cylinder near a rigid bed, *Adv. Eng. Software* **40**, 1191 (2009).
- [18] B. E. Stewart, M. C. Thompson, T. Leweke, and K. Hourigan, The wake behind a cylinder rolling on a wall at varying rotation rates, *J. Fluid Mech.* **648**, 225 (2010).
- [19] A. Rao, M. Thompson, T. Leweke, and K. Hourigan, The flow past a circular cylinder translating at different heights above a wall, *J. Fluids Struct.* **41**, 9 (2013).
- [20] A. Roshko, A. Steinolfson, and V. Chattoorgoon, Flow forces on a cylinder near a wall or near another cylinder, in *Proceedings of the 2nd US Nation Conference on Wind Engineering Research, Fort Collins, Paper IV-15* (IAWE, Fort Collins, 1975).
- [21] J. Choi and S. Lee, Ground effect of flow around an elliptic cylinder in a turbulent boundary layer, *J. Fluids Struct.* **14**, 697 (2000).
- [22] M. Zdravkovich, Forces on a circular cylinder near a plane wall, *Appl. Ocean Res.* **7**, 197 (1985).
- [23] C. Lei, L. Cheng, and K. Kavanagh, Re-examination of the effect of a plane boundary on force and vortex shedding of a circular cylinder, *J. Wind Eng. Industr. Aerodynam.* **80**, 263 (1999).
- [24] F. Angrilli, S. Bergamaschi, and V. Cossalter, Investigation of wall-induced modifications to vortex shedding from a circular cylinder, *J. Fluids Eng.* **104**, 518 (1982).
- [25] S. Taniguchi and K. Miyakoshi, Fluctuating fluid forces acting on a circular cylinder and interference with a plane wall, *Exp. Fluids* **9**, 197 (1990).
- [26] T. Nishino, G. T. Roberts, and X. Zhang, Unsteady RANS and detached-eddy simulations of flow around a circular cylinder in ground effect, *J. Fluids Struct.* **24**, 18 (2008).

- [27] M. Breuer, Large-eddy simulations of the subcritical flow past a circular cylinder: Numerical and modeling aspects, *Int. J. Numer. Methods Fluids* **28**, 1281 (1998).
- [28] X. Ma, G.-S. Karamanos, and G. E. Karniadakis, Dynamics and low-dimensionality of a turbulent near wake, *J. Fluid Mech.* **410**, 29 (2000).
- [29] D. Goring and V. Nikora, Despiking acoustic doppler velocimeter data, *J. Hydraul. Eng.* **128**, 117 (2002).
- [30] M. Jesson, M. Sterling, and J. Bridgman, Despiking velocity time series—Optimization through the combination of spike detection and replacement methods, *Flow Meas. Instrum.* **30**, 45 (2013).
- [31] L. Cea, J. Puertas, and L. Pena, Velocity measurements on highly turbulent free surface flow using ADV, *Exp. Fluids* **42**, 333 (2007).
- [32] T. Stoesser, S. Kim, and P. Diplas, Turbulent flow through idealized emergent vegetation, *J. Hydraul. Res.* **136**, 1003 (2010).
- [33] S. Bomminayuni and T. Stoesser, Turbulence statistics in an open-channel flow over a rough bed, *J. Hydraul. Eng.* **137**, 1347 (2011).
- [34] D. Kim, T. Stoesser, and J. Kim, The effect of baffle spacing on hydrodynamics and solute transport in serpentine contact tanks, *J. Hydraul. Res.* **51**, 558 (2013).
- [35] S. Kara, T. Stoesser, T. W. Sturm, and S. Mulahasan, Flow dynamics through a submerged bridge opening with overtopping, *J. Hydraul. Res.* **53**, 186 (2015).
- [36] P. Ouro, C. Wilson, P. Evans, and A. Angeloudis, Large-eddy simulation of shallow turbulent wakes behind a conical island, *Phys. Fluids* **29**, 126601 (2017).
- [37] R. McSherry, K. Chua, T. Stoesser, and S. Mulahasan, Free surface flow over square bars at intermediate relative submergence, *J. Hydraul. Res.* **56**, 825 (2018).
- [38] F. Nicoud and F. Ducros, Subgrid-scale stress modeling based on the square of the velocity gradient tensor, *Flow, Turbul. Combust.* **62**, 183 (1999).
- [39] M. Uhlmann, An immersed boundary method with direct forcing for the simulation of particulate flows, *J. Comput. Phys.* **209**, 448 (2005).
- [40] P. Ouro and T. Stoesser, An immersed boundary-based large-eddy simulation approach to predict the performance of vertical axis tidal turbines, *Comput. Fluids* **152**, 74 (2017).
- [41] P. Ouro, B. Fraga, U. López-Novoa, and T. Stoesser, Scalability of an Eulerian-Lagrangian large-eddy simulation solver with hybrid MPI/OpenMP parallelisations, *Comput. Fluids* **179**, 123 (2019).
- [42] M. Cevheri, R. McSherry, and T. Stoesser, A local mesh refinement approach for large-eddy simulations of turbulent flows, *Int. J. Numer. Methods Fluids* **82**, 261 (2016).
- [43] T. Stoesser, Large-eddy simulation in hydraulics: Quo vadis? *J. Hydraul. Res.* **52**, 441 (2014).
- [44] R. Broglia, A. Pascarelli, and U. Piomelli, Large-eddy simulations of ducts with a free surface, *J. Fluid Mech.* **484**, 223 (2003).
- [45] A. Prasad and C. H. Williamson, The instability of the shear layer separating from a bluff body, *J. Fluid Mech.* **333**, 375 (1997).
- [46] M. Rai, A computational investigation of the instability of the detached shear layers in the wake of a circular cylinder, *J. Fluid Mech.* **659**, 375 (2000).
- [47] J. Kim and H. Choi, Instability of the shear layer separating from a circular cylinder, in *Proceedings of the 3rd AFOSR International Conference on DNS/LES* (Greyden Press, Dayton, OH, 2001).
- [48] J. Hunt, A. Wray, and P. Moin, Eddies, streams, and convergence zone in turbulent flows, in *Proceedings of the Summer Program*, Report CTR-S88, NASA Stanford Center for Turbulence Research, 1988, pp. 193–208.
- [49] M. Braza, D. Faghani, and H. Persillon, Successive stages and the role of natural vortex dislocations in three-dimensional wake transition, *J. Fluid Mech.* **439**, 1 (2001).
- [50] C. Norberg, Pressure forces on a circular cylinder in cross flow, in *Proceedings of the IUTAM symposium: Bluff body wakes, dynamics, and instabilities*, Goettingen, Germany (1992).
- [51] Y.-M. Chiew, Flow around horizontal circular cylinder in shallow flows, *J. Waterway Port Coast. Ocean Eng.* **117**, 25657 (1991).

- [52] H. Jiang, L. Cheng, S. Draper, and H. An, Two- and three-dimensional instabilities in the wake of a circular cylinder near a moving wall, *J. Fluids Mech.* **812**, 435 (2017).
- [53] A. Grass, P. Raven, R. Stuart, and J. Bray, The influence of boundary layer velocity gradients and bed proximity on vortex shedding from free spanning pipelines, *J. Energy Resour. Technol.* **106**, 70 (1984).